

The Host Galaxies of Active Galactic Nuclei with Direct Black Hole Mass Measurements*

VARDHA N. BENNERT,¹ NICO WINKEL,² TOMMASO TREU,³ XUHENG DING,⁴ VIVIAN U,^{5,6} RAYMOND P. REMIGIO,⁶ AARON J. BARTH,⁶ MATTHEW A. MALKAN,³ LIZVETTE VILLAFÁÑA,¹ SAMANTHA ALLEN,¹ ELLIE JOHNSON,¹ SEBASTIAN CONTRERAS,^{1,7} MINJIN KIM,^{8,9} SIMON BIRRER,¹⁰ KNUD JAHNKE,² AND SHAOPING ZHENG⁴

¹Physics Department, California Polytechnic State University, San Luis Obispo, CA 93407, USA

²Max-Planck-Institut für Astronomie, Königstuhl 17, D-69117 Heidelberg, Germany

³Department of Physics and Astronomy, University of California, Los Angeles, 430 Portola Plaza, Los Angeles, CA 90095, USA

⁴School of Physics and Technology, Wuhan University, Wuhan 430072, China

⁵IPAC, California Institute of Technology, 1200 E. California Blvd., Pasadena, CA 91125, USA

⁶Department of Physics and Astronomy, 4129 Frederick Reines Hall, University of California, Irvine, CA 92697, USA

⁷Department of Astronomy, San Diego State University, San Diego, CA 92182, USA

⁸Kyungpook National University, Daegu 41566, Republic of Korea

⁹Department of Astronomy, Yonsei University, 50 Yonsei-ro, Seodaemun-gu, Seoul 03722, Republic of Korea

¹⁰Department of Physics and Astronomy, Stony Brook University, Stony Brook, NY 11794, USA

ABSTRACT

Reverberation mapping (RM) determines the mass of black holes (BH) in active galactic nuclei (AGNs) by resolving the BH gravitational sphere of influence in the time domain. Recent RM campaigns yielded direct BH masses through dynamical modeling for a sample of 32 objects, spanning a wide range of AGN luminosities and BH masses. In addition, accurate BH masses have been determined by spatially resolving the broad-line region with GRAVITY for a handful of AGNs. Here, we present a detailed analysis of *Hubble Space Telescope* images using surface-brightness profile fitting with state-of-the-art programs. We derive AGN luminosity and host-galaxy properties, such as radii and luminosities for spheroid, disk, and bar (if present). The spheroid effective radii were used to measure stellar velocity dispersion from integral-field spectroscopy. Since the BH masses of our sample do not depend on any assumption of the virial factor needed in single-epoch spectroscopic mass estimates, we can show that the resulting scaling relations between the mass of the supermassive BHs and their host galaxies match those of quiescent galaxies, naturally extending to lower masses in these (predominantly) spiral galaxies. We find that the inner AGN orientation, as traced by the broad-line region inclination angle, is uncorrelated with the host-galaxy disk. Our sample has the most direct and accurate M_{BH} measurements of any AGN sample and provides a fundamental local benchmark for studies of the evolution of massive black holes and their host galaxies across cosmic time.

Keywords: Active galactic nuclei (16), AGN host galaxies (2017), Active galaxies (17), Supermassive black holes (1663), Scaling relations (2031), Seyfert galaxies (1447), Galaxy evolution (594), Black hole physics (159)

1. INTRODUCTION

Supermassive black holes (SMBHs) are common in the centers of massive galaxies. Their masses (M_{BH}) correlate with the properties of their host galaxies, such as stellar mass, spheroid luminosity, and stellar velocity dispersion σ_* (e.g., Magorrian et al. 1998; Gebhardt et al. 2000; Ferrarese & Merritt 2000). The tightness of the M_{BH} –host galaxy relations (~ 0.4 dex) over a large range of masses indicates that the formation and evolution of galaxies is linked to that of black holes (BHs). Mechanisms explaining the co-evolution of SMBHs and

Corresponding author: Vardha N. Bennert
 vbenner@calpoly.edu

* Based on observations made with the NASA/ESA Hubble Space Telescope, obtained at the Space Telescope Science Institute, which is operated by the Association of Universities for Research in Astronomy, Inc., under NASA contract NAS5-26555. These observations are associated with programs # 17103 and 17063.

their host galaxies involve feedback from Active Galactic Nuclei (AGNs; e.g., Di Matteo et al. 2005; Fabian 2012; Hopkins et al. 2016; Morganti 2017) and hierarchical growth through major mergers (Peng 2007; Jahnke & Macciò 2011). Despite many observational studies, both in the local universe and across cosmic history (for reviews, see, e.g., Ferrarese & Ford 2005; Kormendy & Ho 2013; Heckman & Best 2014; Graham 2016), open questions remain, such as the origin and drivers of the relations, the role of host-galaxy morphology, and the evolution of the relations with cosmic time. To make progress, it is essential to understand systematic uncertainties, and measure both M_{BH} and host properties as robustly as possible in the local universe, which serves as an anchor for high-redshift studies.

In local quiescent galaxies, the gravitational sphere of influence of the SMBH can be spatially resolved by tracing the motion of stars and gas in the center, resulting in an estimate of M_{BH} . For more distant galaxies, reverberation mapping (RM) of accreting SMBHs in type-1 AGNs resolves the gravitational sphere of influence of the BH in the time domain (e.g., Wandel et al. 1999; Vestergaard 2002), using gas in the vicinity of the BH, the broad-line region (BLR). The BLR gas is photoionized by the AGN accretion disk continuum. It emits Doppler-broadened lines (e.g., Hydrogen) upon recombination, the velocity of their broadening assumed to be accelerated primarily by the gravity of the nearby SMBH. In RM, the time-delayed response of the BLR to ionizing radiation from the central accretion disk is monitored. The time lag between ionizing continuum changes and corresponding BLR changes measures the light-crossing time and thus, the characteristic size of the BLR. When combined with the velocity of the gas, as traced by the broad emission line width, M_{BH} can be estimated up to the “virial” factor f that depends on the unknown geometry and kinematic structure of the BLR: $M_{\text{BH}} = f R_{\text{BLR}} V^2 / G$ (f = virial factor, R_{BLR} = BLR radius, V = broad-line width, and G = gravitational constant).

A sample-averaged f value has typically been estimated by matching the $M_{\text{BH}}-\sigma_*$ relation of active galaxies to that of quiescent galaxies (e.g., Onken et al. 2004; Woo et al. 2010; Park et al. 2012). The importance of the AGN sample with M_{BH} based on RM (the “RM sample”) lies in determining an empirical relation between BLR size and accretion-disk luminosity (e.g., Bentz et al. 2013). This size-luminosity relation enables rough estimates of single-epoch M_{BH} masses of hundreds of thousands of AGNs across cosmic history (e.g., Shen et al. 2011; Willott et al. 2010; Mortlock et al. 2011; Rakshit et al. 2020), to study the cosmic evolution of the

M_{BH} scaling relations (e.g., Treu et al. 2004; Bennert et al. 2010; Ding et al. 2021), and has been used in recent JWST discoveries of SMBHs at very high redshift (e.g., Pacucci & Loeb 2024; Greene et al. 2024).

Recent progress has enabled direct M_{BH} measurements by forward modeling the BLR emission. Our team has been using the Code for AGN Reverberation and Modeling of Emission Lines (CARMEL) (e.g., Brewer et al. 2011; Pancoast et al. 2011, 2014, 2018; Williams et al. 2018; Villafañá et al. 2022; Bentz et al. 2022, 2023a,b). Based on a Bayesian framework, CARMEL explores a 27-parameter space that incorporates M_{BH} and various geometric and dynamical properties of the BLR. It determines the combination of model parameters that best fits the RM data, creating a 3D map of the high-speed gas that surrounds the BH. Importantly, this method provides the most precise M_{BH} in AGNs, without the need of invoking the virial factor. Note that other teams have developed similar codes for the same purpose, such as BRAINS (Li et al. 2013, 2018; Stone et al. 2025) and GRAVITY (GRAVITY Collaboration et al. 2018, 2021a,b).

The CARMEL sample has grown to 32 AGNs, spanning a wide range of luminosities and BH masses ($6.4 < \log M_{\text{BH}}/M_{\odot} < 9.1$). In addition, for a handful of AGNs, accurate M_{BH} has been determined by spatially resolving (and modeling) the BLR with GRAVITY at the Very Large Telescope Interferometer (VLTI GRAVITY Collaboration et al. 2018, 2021a,b).

Of the observed M_{BH} –host galaxy scaling relations, the one between BH mass and stellar velocity dispersion, $M_{\text{BH}}-\sigma_*$, is of particular interest, since it has been used to determine the sample-averaged virial factor for RM AGNs. However, it is known that σ_* can vary significantly across definitions common in the literature. Measurements depend on the aperture used, the effects of inclination, the presence of a kinematically cold, rotating disk and, for type-1 AGN, the non-stellar continuum outshining the underlying stellar continuum and its absorption lines (e.g., Debattista et al. 2013; Hartmann et al. 2014; Bennert et al. 2015). These uncertainties caution the use of σ_* determined from long-slit spectroscopy or fibers. Integral-field unit (IFU) spectroscopy is the best way forward towards a precise measurement of σ_* , using spatially resolved kinematics and integrating over the effective radius.

Our team obtained IFU data with Keck/KCWI and VLT/MUSE for the RM sample with directly measured M_{BH} (Winkel et al. 2025; Remigio et al. 2025). The IFU observations map stellar kinematics across the galaxy and spheroid effective radii. After accounting for different M_{BH} distributions, we can demonstrate directly that

AGNs follow the same $M_{\text{BH}}-\sigma_*$ relation as quiescent galaxies. Fitting the derived $M_{\text{BH}}-\sigma_*$ relation yields the same virial factor f as from the classical method, as well as the average of individual f -factors from dynamical modeling ($\log f_{\text{dyn}} = 0.66 \pm 0.07$, [Winkel et al. 2025](#)). The $M_{\text{BH}}-\sigma_*$ relation is robust, regardless of host-galaxy morphology, and there is no significant dependence of the sample-average f -factor on host-galaxy morphology ([Winkel et al. 2025](#)).

The stellar velocity dispersion measurements presented in [Winkel et al. \(2025\)](#) are integrated over effective radii of the spheroid and/or total host galaxy. In this paper, we describe the detailed analysis of the AGN host galaxies that led to the measurements of these effective radii (and thus stellar-velocity dispersion). We present high resolution and high signal-to-noise (S/N) Hubble Space Telescope (HST) images of the RM and GRAVITY sample with directly measured M_{BH} . The image analysis uses state-of-the-art programs (`galight` and `lenstronomy`) to derive host-galaxy properties, such as luminosities, radii, and morphologies. When combined with the directly measured BH masses, we can create the full range of M_{BH} –host galaxy scaling relations. Using BLR modeling results, we can compare the inclination between BLR and host-galaxy disk, to study their relative orientations which provides clues to SMBH feeding.

The paper is organized as follows. Sample selection is summarized in Section 2. HST observations and data reduction are presented in Section 3. Surface-brightness profile modeling is described in Section 4. Results are discussed in Section 5. The paper concludes with a summary and outlook (Section 6). Appendix A presents details of surface-brightness fitting results.

Throughout this paper, we adopt $H_0 = 67.8 \text{ km s}^{-1} \text{ Mpc}^{-1}$, $\Omega_m = 0.308$, and $\Omega_\Lambda = 0.692$ ([Planck Collaboration et al. 2016](#)).

2. SAMPLE SELECTION AND BH MASSES

The sample consists of 32 local RM AGNs with directly measured M_{BH} from dynamical modeling (Table 3; for details, see Table 2 in [Villafañá et al. 2023](#)).¹¹ This sample has the most robust M_{BH} measurements in AGNs, as it does not rely on the assumption of a virial factor. The low-redshift ($0.01 \leq z \leq 0.16$) sample covers a large range in AGN luminosities and BH masses ($\log L_{\text{bol}}/\text{erg s}^{-1} \sim 10^{43-47}$, $\log M_{\text{BH}}/\text{M}_\odot \sim 6.4-8.3$, [Winkel et al. 2025](#)). We include five AGNs for which accurate M_{BH} have been determined by spatially resolving the BLR with GRAVITY. Two of these five GRAVITY AGNs have both CARAMEL RM and GRAVITY measurements: NGC 3783 and IC 4329A. Note that while the GRAVITY collaboration has published results for a total of seven local AGNs so far, we include only those with existing IFU and HST data.

Finally, we include nine AGNs for which the BH mass has been determined through classical RM (cRM), but for which the data were not of sufficient quality for dynamical modeling. For these objects, we adopt a virial factor of $\log f = 0.65$ to re-calculate M_{BH} . This value is consistent with the average of the individual values of $\log f_{\text{dyn}} = 0.66 \pm 0.07$ determined in [Winkel et al. \(2025\)](#) (see also [Villafañá et al. 2023](#)). The final sample thus consists of 44 objects. The most important sample parameters are listed in Tables 1 and 3; further details are given by [Winkel et al. \(2025\)](#). As our comparison sample, we use 51 quiescent galaxies (either ellipticals or spirals/S0 with classical bulges) with M_{BH} based on dynamical modeling of spatially resolved stellar kinematics from [Kormendy & Ho \(2013, hereafter KH13\)](#). For details on the quiescent sample, see Section 3.4 in [Bennert et al. \(2021\)](#). KH13 lists spheroid magnitudes in the V band as well as colors, which were used to calculate the I -band luminosities as described by [Bennert et al. \(2021\)](#).

Table 1. Sample Properties and HST Observations

AGN Name	R.A. (J2000)	Decl. (J2000)	z	Instrument	Filter	Program ID	Reference
(1)	(2)	(3)	(4)	(5)	(6)	(7)	(8)
Mrk 335	00:06:19.52	+20:12:10.5	0.0258	WFC3/UVIS	F814W	17103	B26

Table 1 *continued*

¹¹ Note that for three of these AGNs, Ark 120, Mrk 110, and Mrk 142, BLR models fit the data only with moderate quality

([Villafañá et al. 2022](#)), and have not been further included in CARAMEL-extended sample papers. We include these objects here, but our results do not change if we exclude them.

Table 1 (*continued*)

AGN Name	R.A.	Decl.	<i>z</i>	Instrument	Filter	Program ID	Reference
	(J2000)	(J2000)					
(1)	(2)	(3)	(4)	(5)	(6)	(7)	(8)
Mrk 1501	00:10:31.01	+10:58:29.5	0.087	ACS/WFC1	F814W	15444	K21
Zw 535-012	00:36:20.93	+45:39:53.7	0.0476	ACS/WFC1	F814W	15444	K21
Mrk 590	02:14:33.56	-00:46:00.2	0.0261	ACS/HRC	F550M	9851	B06
Mrk 1044	02:30:05.52	-08:59:53.2	0.0161	ACS/WFC1	F814W	15444	K21
Mrk 1048	02:34:37.77	-08:47:15.4	0.0427	ACS/WFC1	F814W	15444	K21
3C 120	04:33:11.10	+05:21:15.6	0.033	ACS/HRC	F550M	9851	B06
Ark 120	05:16:11.42	-00:08:59.4	0.0327	ACS/WFC1	F814W	15444	K21
NGC 2617	08:35:38.80	-04:05:17.9	0.0142	WFC3/UVIS	F547M	13816	B18
IRAS 09149-6206	09:16:09.39	-62:19:29.9	0.0573	WFC3/UVIS	F814W	17103	B26
MCG +04-22-042	09:23:43.00	+22:54:32.6	0.0332	ACS/WFC1	F814W	15444	K21
Mrk 110	09:25:12.85	+52:17:10.4	0.0355	ACS/HRC	F550M	9851	B06
Mrk 1239	09:52:19.16	-01:36:44.1	0.0196	WFPC2/PC1	F606W	5479	M98
Mrk 141	10:19:12.56	+63:58:02.8	0.0417	WFC3/UVIS	F814W	17103	B26
NGC 3227	10:23:30.58	+19:51:54.3	0.0038	WFC3/UVIS	F547M	11661	B18
Mrk 142	10:25:31.28	+51:40:34.9	0.0446	WFC3/UVIS	F547M	11662	B13
NGC 3516	11:06:47.49	+72:34:06.9	0.0088	WFC3/UVIS	F547M	11661	B18
SBS 1116+583A	11:18:57.69	+58:03:23.7	0.0279	WFC3/UVIS	F547M	11662	B13
Arp 151	11:25:36.17	+54:22:57.0	0.0207	WFC3/UVIS	F547M	11662	B13
NGC 3783	11:39:01.76	-37:44:19.2	0.0097	WFC3/UVIS	F547M	11661	B18
Mrk 1310	12:01:14.36	-03:40:41.1	0.0195	WFC3/UVIS	F547M	11662	B13
NGC 4151	12:10:32.58	+39:24:20.6	0.0033	WFC3/UVIS	F547M	11661	B18
PG 1211+143	12:14:17.67	+14:03:13.2	0.081	ACS/HRC	F550M	10833	B09a
Mrk 50	12:23:24.14	+02:40:44.8	0.0234	WFC3/UVIS	F814W	16014	B26
NGC 4593	12:39:39.43	-05:20:39.3	0.0083	WFC3/UVIS	F547M	11661	B18
PG 1310-108	13:13:05.79	-11:07:42.4	0.0343	WFC3/UVIS	F814W	17103	B26
RBS 1303	13:41:12.90	-14:38:40.6	0.0418	WFC3/UVIS	F814W	17103	B26
IC 4329A	13:49:19.26	-30:18:34.2	0.0151	ACS/HRC	F550M	10516	B09a
Mrk 279	13:53:03.45	+69:18:29.6	0.0305	WFC3/UVIS	F814W	17103	B26
NGC 5548	14:17:59.54	+25:08:12.6	0.0163	WFC3/UVIS	F547M	11661	B18
PG 1426+015	14:29:06.57	+01:17:06.2	0.086	WFPC2/PC1	F547M	10833	B09a
Mrk 841	15:04:01.20	+10:26:16.2	0.0364	WFC3/UVIS	F814W	17103	B26
Mrk 1392	15:05:56.55	+03:42:26.3	0.0359	WFC3/UVIS	F814W	17103	B26
Mrk 1511	15:31:18.07	+07:27:27.9	0.0339	WFC3/UVIS	F547M	13816	B18
PG 1617+175	16:20:11.28	+17:24:27.5	0.112	WFPC2/PC1	F547M	10833	B09a
NPM 1G+27.0587	18:53:03.87	+27:50:27.7	0.062	WFC3/UVIS	F814W	17103	B26
Zw 229-015	19:05:25.94	+42:27:39.7	0.0279	ACS/WFC1	F814W	15444	K21
NGC 6814	19:42:40.64	-10:19:24.6	0.0052	WFC3/UVIS	F814W	12961	B19
RXJ 2044.0+2833	20:44:04.50	+28:33:12.1	0.05	ACS/WFC1	F814W	15444	K21
Mrk 509	20:44:09.75	-10:43:24.7	0.0347	WFC3/UVIS	F547M	12212	F13
PG 2130+099	21:32:27.81	+10:08:19.5	0.064	ACS/HRC	F550M	9851	B06
PG 2209+184	22:11:53.89	+18:41:49.9	0.07	WFC3/UVIS	F814W	17103	B26
RBS 1917	22:56:36.50	+05:25:17.2	0.065	WFC3/UVIS	F814W	17103	B26
NGC 7469	23:03:15.67	+08:52:25.3	0.0166	WFC3/UVIS	F547M	11661	B18

Table 1 *continued*

Table 1 (*continued*)

AGN Name	R.A. (J2000)	Decl. (J2000)	z	Instrument	Filter	Program ID	Reference
(1)	(2)	(3)	(4)	(5)	(6)	(7)	(8)

NOTE— Col. (1): AGN Name. Col. (2): Right ascension in hours, minutes and seconds (NED). Col. (3): Declination in degrees, arcminutes and arcseconds (NED). Col. (4): Redshift (NED). Col. (5): Instrument and aperture. Col. (6): Filter. Col. (7): Program ID. Col. (8): Original paper: B08: [Bennert et al. \(2008\)](#); B26: this paper; B06: [Bentz et al. \(2006\)](#); B09a: [Bentz et al. \(2009\)](#); B13: [Bentz et al. \(2013\)](#); B18: [Bentz & Manne-Nicholas \(2018\)](#); C07: [Canalizo et al. \(2007\)](#); F13: [Fischer et al. \(2013\)](#); K21: [Kim et al. \(2021\)](#); M98: [Malkan et al. \(1998\)](#).

3. HUBBLE SPACE TELESCOPE OBSERVATIONS AND DATA REDUCTION

The HST data are a combination of newly conducted observations (PI Bennert; GO 17103; 11 objects), as well as archival images obtained from different programs. For program GO 17103, each object was observed for one orbit with WFC3 in filter F814W. Long exposures (500–600 s) were complemented with short, unsaturated ones (10 s), for a full dynamic range. The observing sequence (short, long, long – dither – long, long, short) minimizes buffer dump, using a manual dither pattern corresponding to the “WFC3-UVIS-GAPLINE”. Archival images were obtained using WFPC2, ACS or WFC3 in medium or broad band V or I filters. Details on the observations are given in Table 1.

All data are reduced and analyzed in a homogeneous way, using the standard HST calibration pipeline. In addition, **LA-Cosmic** ([van Dokkum 2001](#)) was run before image combination to improve cosmic ray rejection. For those objects for which the central AGN point source was saturated in the long exposures, short exposures, scaled by exposure time, were used to replace the saturated pixels. Long exposures were dither-combined using the package **AstroDrizzle**. Various drizzle parameters (e.g., scale and pixfrac) were applied to find the best settings, based on the resulting resolution and image quality. In the ACS archival dataset (GO 15444), the short-exposure sub-array images were affected by bias striping noise, which was mitigated using the **acs_desstripe_plus** task ([Grogin et al. 2010, 2011; Kim et al. 2021](#)). Resulting images are of high quality, both in terms of resolution and S/N.

4. HOST GALAXY SURFACE-BRIGHTNESS FITTING

HST images were analyzed using the 2D host-galaxy fitting software **lenstronomy** ([Birrer & Amara 2018; Birrer et al. 2021](#)), in combination with **galight** ([Ding et al. 2020](#)). **Lenstronomy** is a modern version of **GALFIT** ([Peng et al. 2002](#)), allowing for a more gen-

eral surface-brightness reconstruction with coefficients determined through linear minimization rather than a non-linear parameter fitting. The Markov Chain Monte Carlo (MCMC) technique provides realistic errors and explores the covariance between various model parameters. **Lenstronomy** was designed for galaxy lensing, but can be applied broadly for general 2D galaxy decompositions. The source code is public (see *Astrophysics Source Code Library*) and can be directly modified by the user. The **galight** software package offers a user-friendly application of **lenstronomy** and includes helpful tools to extract Point Spread Function (PSF) stars, create masks, and subtract the background.

For each object, the full data analysis includes the following steps (see also [Bennert et al. 2021](#), for further details on the general procedure):

(1) PSF stars are chosen from stars in the field of view (FOV). Ideally, these stars are bright, but not saturated, and close to the AGN location in the FOV. A library of PSF stars is created from suitable stars in all available exposures. Multiple PSF stars from different images (obtained with the same camera, in the same filter, at the same orientation and close in time) are combined into one high S/N PSF, through an iterative PSF reconstruction (e.g., [Birrer et al. 2019; Shajib et al. 2019, 2020](#), available on [github](#) as **psfr**).

(2) The final-reduced image of the AGN host galaxy is examined to determine morphology and components fitted (spheroid, disk, bar). For objects for which there is at least an indication of a visual bar, the bar parameters size, position angle, and ellipticity are determined manually and used as starting parameters for the bar in the spheroid–disk–bar fit.

(3) The sky background is subtracted.

(4) A noise-level map is created, taking into account the dithering process.

(5) A spherical image cut-out is created, centered on the AGN. Nearby objects are masked or fitted simultaneously, depending on brightness and proximity to, or overlap with, the AGN host galaxy.

(6) For each object, the central AGN is fitted with a point source (PSF). The host galaxy is fitted with

three different models: (a) a spheroid-only component (free Sérsic index with $1 \leq n \leq 5$); (b) a spheroid plus disk component (Sérsic index $n = 1$; if present); (c) a spheroid plus disk plus bar component (elliptical Sérsic model with $n = 0.5$; if present). Based on pre-defined starting parameters and constraints, `lenstronomy` uses a Particle Swarm Optimizer (PSO) as a minimizer and an MCMC sampler to calculate the posterior distribution of the parameter space. We experiment with different settings for the PSO (number of particles and iterations). For all fits, we plot the PSO particle positions, parameter velocity and inferred flux as a function of iteration to ensure that the chain converged.

(7) We first run the spheroid-only fit. This fit is robust and gives the same results independent of starting parameters used.

(8) We then use the results from the spheroid-only fit as starting parameters for the disk in the subsequent spheroid–disk and spheroid–disk–bar fit (if required). (a) For the spheroid–disk fit, we force the disk to be larger than the spheroid and more elliptical. Three different starting parameters are used for both the spheroid and disk effective radius (see Table 2). In combination, this results in nine different models that are run, ensuring a true global minimum is reached in the best fit. (b) For the spheroid–disk–bar fit, we force the disk to be larger than the bar and the spheroid, and the spheroid component to be the most round one of three components. The same starting parameters are used for spheroid and disk as above (8a), with the bar added with specific starting parameters (radius and position angle) determined visually.

(9) Through careful inspection and comparison of the fits for the different runs (such as residual plots, final results, chi-square values, uncertainties), we determine the best model and fit for all objects.

(10) The fits are used to distinguish between classical and pseudo-bulges. We use the Sérsic index as a first indicator, but conservatively, take into account other parameters as well (presence of bar, inclination, spheroid-to-total luminosity ratio, rotation; discussed in detail in Section 5.1).

(11) Galactic foreground extinction is subtracted using the dust extinction map (Schlafly & Finkbeiner 2011).

(12) Standard cosmology is applied to convert arcsecond radii to parsec and apparent magnitudes to luminosities. The k -correction uses `PySynphot` and an Sa galaxy template (Kinney et al. 1996). The F814W filter magnitudes are virtually identical to I -band magnitudes (Harris 2018), given the colors of all galaxy templates. Based on the different fitting results (using dif-

ferent starting parameters and PSFs etc.), we conservatively adopt 0.04 dex as uncertainty on the derived luminosities.

General notes on the modelling procedure and results: (1) The central AGN point source was fitted with a PSF. (a) While the HST PSF has a full width at half maximum (FWHM) of ~ 2.5 pixels, it extends outwards by several arcseconds and includes diffraction spikes and sometime ghosts. However, 98% of the encircled energy is within 2 arcseconds (for details, see Sections 6.6.1–6.6.3 in the WFC3 Instrument Handbook; Pagul & Rivera 2024). (b) In some sources, the AGN position is offset from the centroid of the host-galaxy spheroid component by $0.^{\prime\prime}1$ – $0.^{\prime\prime}2$. Such offsets can be caused by central dust lanes, which are commonly seen in these type-1 Seyfert galaxies, or by the intrinsic asymmetry common in AGN hosts, and due to recent mergers or interactions (for discussions, see, e.g., Kim et al. 2017). (2) In many objects, residuals of rings and spiral arms remain after the fitting. This is a natural consequence of fitting intrinsically asymmetric features such as spiral arms, or asymmetries caused by mergers or interactions with spherically symmetric models with a limited number of components (i.e., AGN, spheroid, disk, bar, if present). While increasing the number of components and/or including special functions (such as a hyperbolic tangent rotation function) with Fourier modes would allow us to fit these asymmetries and measure asymmetry parameters (Kim et al. 2017), this is beyond the scope of our paper. Physical quantities relevant to this paper, such as the radii of the spheroid and disk as well as the magnitudes can be robustly inferred by the physically-motivated models we chose. (3) For NGC 4593, the HST FOV is too small and mostly covers the bar. While spheroid and bar component are reliably fitted, the disk fit (which is much larger than the FOV) is unreliable. (4) For Mrk 279, the bottom chip was affected by a strong “ghost” and thus masked out and excluded from the fitting.

5. RESULTS AND DISCUSSION

5.1. Host Galaxy Morphology

By visual inspection of the images and residuals of the surface-brightness fitting, host-galaxy morphologies were determined. Results of the surface-brightness fitting are shown in Appendix A. Table 3, column 7, lists the host-galaxy morphology.

Of our sample of 44 AGNs, only five objects (11%) are hosted by bona-fide elliptical galaxies. The majority of AGNs (39/44; 89%) are hosted by spiral or S0 galaxies. Of the disk galaxies, 18/39 (46%) were best fitted with an additional bar component. Seyfert galax-

Table 2. Starting Parameters for Spheroid-Disk Fit

Disk effective radius R_{disk}	Spheroid effective radius R_{sph}
(1)	(2)
R_{SS}	0.2 R_{SS}
	0.5 R_{SS}
	0.75 R_{SS}
0.5 R_{SS}	0.1 R_{SS}
	0.25 R_{SS}
	0.375 R_{SS}
2 R_{SS}	0.4 R_{SS}
	R_{SS}
	1.5 R_{SS}

NOTE— To ensure a true global minimum is reached, we choose a series of nine different starting parameters for the effective radii of the spheroid+disk fit, relative to the effective radius derived from the best fitting single Sérsic profile R_{SS} from the spheroid-only fit. For the spheroid+disk+bar fit, the same combination is used, with the bar added with specific starting parameters (radius and position angle) as determined visually. Col. (1): Starting parameters for disk effective radius R_{disk} . Col. (2): Starting parameters for spheroid effective radius R_{sph} .

ies are generally considered to have similar bar fractions as quiescent spiral galaxies (see, e.g., Hunt & Malkan 1999): 1/3 no bar, 1/3 weak bar (“SAB”), and 1/3 with a strong bar (“SB”). Thus, we are likely missing a small fraction of weak bars due to dust obscuration in the optical, especially in highly inclined disks.

Two objects (5%) show strong signs of merger activity, Mrk 1048 and Arp 151. The HST image of

Mrk 1048 reveals two nuclei and a tidal tail forming a central ring structure; the latter had been noted previously and interpreted as evidence of merger activity (Parker et al. 2014). The HST image of Arp 151 shows a highly elongated one-sided tidal tail-like structure with a second nucleus. A handful of other objects (such as Mrk 1501, 3C 120, Ark 120, IRAS 09149-6206, PG 1310-108, Mrk 279, NPM 1G+27.0587) show asymmetries, nearby neighbors, or tidal tails. Overall, the distribution of host-galaxy morphologies is typical for Seyfert-type AGNs (e.g., Kocevski et al. 2012; Schawinski et al. 2012; Marian et al. 2019; Husemann et al. 2022; Bennert et al. 2021; Kim et al. 2017, 2021), and also low-redshift PG quasars (e.g., Zhao et al. 2021).

For all galaxies fitted by either spheroid+disk or spheroid+disk+bar, we classify the spheroid as pseudo-bulge, if at least three of the following four criteria are met (Kormendy & Ho 2013; Bennert et al. 2021): (1) Sérsic index < 2 ; (2) spheroid-to-total luminosity ratio < 0.5 ; (3) rotation dominated, i.e., ratio between maximum rotational velocity (corrected for inclination) at effective spheroid radius and central stellar-velocity dispersion > 1 ; (4) for face-on galaxies, the presence of a bar is considered an indicator for the existence of a pseudo-bulge. Of the late-type galaxies, 23/40 (58%) have been found to harbor pseudo-bulges in this way (see Table 3). This fraction is similar to a sample of both local type-1 AGNs and low-redshift PG quasars (Bennert et al. 2021; Zhao et al. 2021).

Table 3. Black Hole Masses and Derived Host Galaxy Properties

AGN Name	M_{BH}	L_{sph}	$L_{\text{sph+bar}}$	L_{disk}	L_{host}	Host	i_{host}	i_{BLR}	σ_{BLR}	Sample	Reference
(1)	(2)	(3)	(4)	(5)	(6)	(7)	(8)	(9)	(10)	(11)	(12)
Mrk 335	$7.25^{+0.1}_{-0.1}$	9.86	...	9.65	10.07	BD(C)	25	35^{+4}_{-5}	38^{+5}_{-5}	CARAMEL	G17
Mrk 1501	$7.86^{+0.2}_{-0.17}$	10.56	...	10.49	10.82	BD(C)	44	20^{+5}_{-6}	22^{+12}_{-6}	CARAMEL	G17
Zw 535-012	$7.57^{+0.15}_{-0.1}$	9.79	10.39	10.20	10.62	BDB(P)	60	cRM	U22**
Mrk 590	$7.58^{+0.07}_{-0.07}$	9.83	...	9.85	10.14	BD(C)	42	cRM	M21**
Mrk 1044	$6.1^{+0.12}_{-0.1}$	9.46	9.87	9.66	10.09	BDB(P)	29	cRM	D15**
Mrk 1048	$7.79^{+0.44}_{-0.48}$	10.35	...	10.83	10.95	BD(P)	48	22^{+9}_{-9}	31^{+14}_{-10}	CARAMEL	V22
3C 120	$7.84^{+0.14}_{-0.19}$	9.64	9.64	B(C)	...	18^{+5}_{-3}	21^{+8}_{-5}	CARAMEL	G17
Ark 120	$8.26^{+0.12}_{-0.17}$	10.63	...	10.24	10.78	BD(C)	31	14^{+4}_{-3}	32^{+7}_{-8}	CARAMEL ¹	V22
NGC 2617	$7.51^{+0.47}_{-0.47}$	9.12	...	10.09	10.13	BD(C)	19	cRM	F17**
IRAS 09149-6206	$8.0^{+0.3}_{-0.4}$	10.47	...	10.61	10.84	BD(P)	51	35^{+13}_{-10}	61^{+20}_{-20}	GRAVITY	G20

Table 3 *continued*

Table 3 (*continued*)

AGN Name	M_{BH}	L_{sph}	$L_{\text{sph+bar}}$	L_{disk}	L_{host}	Host	i_{host}	i_{BLR}	ϕ_{BLR}	Sample	Reference
	(log M_{\odot})	(log L_{\odot})	(log L_{\odot})	(log L_{\odot})	(log L_{\odot})		($^{\circ}$)	($^{\circ}$)	($^{\circ}$)		
(1)	(2)	(3)	(4)	(5)	(6)	(7)	(8)	(9)	(10)	(11)	(12)
MCG +04-22-042	7.59 $^{+0.42}_{-0.28}$	9.92	10.09	10.55	10.70	BDB(P)	58	11 $^{+6}_{-5}$	14 $^{+7}_{-5}$	CARAMEL	V22
Mrk 110	7.17 $^{+0.67}_{-0.26}$	9.57	9.57	B(C)	...	20 $^{+10}_{-11}$	27 $^{+16}_{-13}$	CARAMEL ¹	V22
Mrk 1239	7.47 $^{+0.15}_{-0.92}$	9.25	...	9.55	9.73	BD(P)	43	11 $^{+6}_{-3}$	42 $^{+18}_{-15}$	GRAVITY	G24
Mrk 141	7.46 $^{+0.15}_{-0.21}$	9.85	10.12	10.54	10.69	BDB(P)	40	26 $^{+6}_{-4}$	15 $^{+4}_{-2}$	CARAMEL	W18
NGC 3227	7.04 $^{+0.11}_{-0.11}$	8.55	...	9.31	9.38	BD(C)	67	33 $^{+14}_{-9}$	65 $^{+18}_{-12}$	CARAMEL	B23a
Mrk 142	6.23 $^{+0.3}_{-0.3}$	9.35	9.76	9.69	10.03	BDB(P)	36	41 $^{+21}_{-11}$	30 $^{+14}_{-12}$	CARAMEL ¹	L18
NGC 3516	7.61 $^{+0.3}_{-0.7}$	9.59	9.87	9.77	10.13	BDB(P)	35	cRM	D18**
SBS 1116+583A	6.99 $^{+0.32}_{-0.25}$	8.85	9.15	9.65	9.78	BDB(P)	29	18 $^{+8}_{-6}$	22 $^{+11}_{-8}$	CARAMEL	P14
Arp 151	6.62 $^{+0.1}_{-0.13}$	9.28	...	9.24	9.56	BD(C)	71	25 $^{+3}_{-3}$	26 $^{+4}_{-4}$	CARAMEL	P14
NGC 3783	7.45 $^{+0.07}_{-0.1}$	8.99	9.28	9.99	10.13	BDB(P)	29	18 $^{+5}_{-6}$	35 $^{+6}_{-10}$	CARAMEL	B21b
Mrk 1310	7.42 $^{+0.26}_{-0.27}$	9.17	...	9.55	9.70	BD(C)	44	7 $^{+5}_{-2}$	9 $^{+4}_{-2}$	CARAMEL	P14
NGC 4151	7.22 $^{+0.11}_{-0.1}$	9.17	...	9.12	9.45	BD(C)	30	58 $^{+10}_{-8}$	57 $^{+14}_{-16}$	CARAMEL	B22
PG 1211+143	8.07 $^{+0.11}_{-0.15}$	10.13	10.13	B(C)	cRM	K00**
Mrk 50	7.51 $^{+0.06}_{-0.07}$	9.71	...	9.82	10.07	BD(C)	40	20 $^{+6}_{-5}$	14 $^{+5}_{-4}$	CARAMEL	W18
NGC 4593	6.65 $^{+0.27}_{-0.15}$	9.52	9.90	8.33	9.91	BDB(P)	64	32 $^{+19}_{-10}$	43 $^{+22}_{-19}$	CARAMEL	W18
PG 1310-108	6.48 $^{+0.21}_{-0.18}$	9.18	9.41	9.91	10.05	BDB(P)	24	44 $^{+35}_{-13}$	58 $^{+25}_{-16}$	CARAMEL	W18
RBS 1303	6.79 $^{+0.19}_{-0.11}$	9.90	10.30	10.62	10.82	BDB(P)	55	29 $^{+8}_{-9}$	34 $^{+9}_{-10}$	CARAMEL	V22
IC 4329A	7.64 $^{+0.53}_{-0.25}$	8.76	...	9.60	9.66	BD(C)	26	40 $^{+27}_{-18}$	69 $^{+15}_{-30}$	CARAMEL	B23b
Mrk 279	7.58 $^{+0.08}_{-0.08}$	10.35	...	10.24	10.60	BD(C)	52	29 $^{+3}_{-3}$	41 $^{+4}_{-4}$	CARAMEL	W18
NGC 5548	7.54 $^{+0.34}_{-0.24}$	10.11	...	9.82	10.29	BD(C)	30	47 $^{+13}_{-16}$	39 $^{+14}_{-14}$	CARAMEL ²	W20
PG 1426+015	9.02 $^{+0.11}_{-0.15}$	10.48	10.48	B(C)	cRM	K00**
Mrk 841	7.62 $^{+0.5}_{-0.3}$	9.87	9.99	10.08	10.35	BDB(P)	19	30 $^{+11}_{-15}$	41 $^{+11}_{-11}$	CARAMEL	V22
Mrk 1392	8.16 $^{+0.11}_{-0.13}$	9.92	10.24	10.67	10.83	BDB(P)	61	26 $^{+3}_{-3}$	41 $^{+5}_{-5}$	CARAMEL	V22
Mrk 1511	7.11 $^{+0.2}_{-0.17}$	9.06	9.98	10.47	10.62	BDB(P)	20	19 $^{+6}_{-5}$	36 $^{+9}_{-10}$	CARAMEL	W18
PG 1617+175	7.69 $^{+0.21}_{-0.38}$	10.27	10.27	B(C)	cRM	H21**
NPM 1G+27.0587	7.64 $^{+0.4}_{-0.36}$	10.10	...	11.00	11.05	BD(P)	39	19 $^{+11}_{-8}$	18 $^{+11}_{-9}$	CARAMEL	V22
Zw 229-015	6.94 $^{+0.14}_{-0.14}$	9.52	10.02	9.85	10.27	BDB(P)	49	33 $^{+6}_{-5}$	34 $^{+6}_{-6}$	CARAMEL	W18
NGC 6814	6.42 $^{+0.24}_{-0.16}$	8.37	8.91	9.52	9.72	BDB(P)	24	49 $^{+20}_{-22}$	50 $^{+22}_{-19}$	CARAMEL	P14
RXJ 2044.0+2833	7.09 $^{+0.17}_{-0.17}$	9.40	10.02	10.21	10.57	BDB(P)	47	42 $^{+10}_{-8}$	51 $^{+15}_{-12}$	CARAMEL	V22
Mrk 509	8.0 $^{+0.06}_{-0.23}$	10.15	...	10.04	10.40	BD(C)	40	69 $^{+6}_{-12}$	64 $^{+11}_{-9}$	GRAVITY	G24
PG 2130+099	6.92 $^{+0.24}_{-0.23}$	9.35	...	9.91	10.02	BD(C)	54	30 $^{+11}_{-10}$	33 $^{+12}_{-12}$	CARAMEL	G17
PG 2209+184	7.53 $^{+0.19}_{-0.2}$	10.62	...	10.23	10.77	BD(C)	30	30 $^{+9}_{-7}$	29 $^{+11}_{-8}$	CARAMEL	V22
RBS 1917	7.04 $^{+0.23}_{-0.35}$	9.31	...	9.91	10.01	BD(P)	26	20 $^{+10}_{-4}$	25 $^{+9}_{-8}$	CARAMEL	V22
NGC 7469	7.18 $^{+0.05}_{-0.09}$	9.71	10.19	9.84	10.37	BDB(P)	37	cRM	L21**

Table 3 *continued*

Table 3 (continued)

AGN Name	M_{BH} ($\log M_{\odot}$)	L_{sph} ($\log L_{\odot}$)	$L_{\text{sph+bar}}$ ($\log L_{\odot}$)	L_{disk} ($\log L_{\odot}$)	L_{host} ($\log L_{\odot}$)	Host	i_{host} ($^{\circ}$)	i_{BLR} ($^{\circ}$)	α_{BLR} ($^{\circ}$)	Sample	Reference
(1)	(2)	(3)	(4)	(5)	(6)	(7)	(8)	(9)	(10)	(11)	(12)

NOTE— Col. (1): AGN Name. Col. (2): Logarithm of M_{BH} (solar units), compiled from literature (see column 12 for references). Col. (3): Logarithm of spheroid luminosity (solar units) (uncertainty of 0.04 dex). Luminosities given in columns (3-6) are either in I band or V band, depending on filter used (see Table 1). Col. (4): Logarithm of spheroid+bar luminosity (solar units) (uncertainty of 0.04 dex). Col. (5): Logarithm of disk luminosity (solar units) (uncertainty of 0.04 dex). Col. (6): Logarithm of host luminosity (solar units) (uncertainty of 0.04 dex). Col. (7): Host-galaxy fit (B: spheroid only, BD: spheroid+disk, BDB: spheroid+disk+bar). In parentheses: Spheroid component: C = classical bulge; P = pseudo-bulge. Col. (8): Host inclination based on disk axis ratio (Eq. 2) (uncertainty of $\pm 5^{\circ}$). Col. (9): BLR inclination from BLR modeling. Col. (10): BLR opening angle from BLR modeling. Col. (11): Sample based on M_{BH} measurement. ¹: For three objects (Ark 120, Mrk 110, and Mrk 142), BLR models fit the data only with moderate quality (Villafañá et al. 2022). ²: For NGC 5548, dynamical BLR modeling was performed for two different data sets, set apart by 6 years (Pancoast et al. 2014; Williams et al. 2020). Results used here are taken from Williams et al. (2020), based on $H\beta$ versus V-band, for consistency. Col. (12): References for M_{BH} measurements and BLR modeling (where applicable). *: For NGC 4593, the HST FOV is too small to cover the entire disk and thus, the disk fit is unreliable. **: Denotes objects for which M_{BH} was re-calculated here, assuming an average $\log f = 0.65$. B21b: Bentz et al. (2021); B23a: Bentz et al. (2023a); B23b: Bentz et al. (2023b); D15: Du et al. (2015); D18: De Rosa et al. (2018); F17: Fausnaugh et al. (2017); G17: Grier et al. (2017); G20: GRAVITY Collaboration et al. (2020); G21b: GRAVITY Collaboration et al. (2021b); G24: GRAVITY Collaboration et al. (2024); H21: Hu et al. (2021); K00: Kaspi et al. (2000); L18: Li et al. (2018); L21: Lu et al. (2021); M21: Mandal et al. (2021); P14: Pancoast et al. (2014); U22: U et al. (2022); V22: Villafañá et al. (2022); W18: Williams et al. (2018); W20: Williams et al. (2020).

5.2. M_{BH} -Spheroid Luminosity Relation

Figure 1 shows the resulting relation between M_{BH} and spheroid luminosity, split into I -band and V -band luminosity, according to the HST filter used. Overall, our AGN sample with directly measured BH masses follows the same M_{BH} -spheroid-luminosity relation as quiescent galaxies, and naturally extends the relation to lower masses, for these (predominantly) spiral host galaxies. We fit the relations using a linear regression, taking into account uncertainties (LinMix; Kelly 2007)

$$\log \left(\frac{M_{\text{BH}}}{M_{\odot}} \right) = \alpha + \beta \log X \quad (1)$$

with X either I -band or V -band luminosities ($L_I^{\text{sph}}/10^{10}L_{\odot}$ or $L_V^{\text{sph}}/10^{10}L_{\odot}$). Overall, the scaling relations between M_{BH} and spheroid luminosity agree for AGNs and quiescent galaxies within the uncertainties (Table 4). This further strengthens the conclusion reached by our previous paper based on the same sample (Winkel et al. 2025), where we demonstrate, for the first time, that AGNs follow the same $M_{\text{BH}}-\sigma_{\star}$ and $M_{\text{BH}}-M_{\text{sph,dyn}}$ relations as quiescent galaxies, regardless of host-galaxy morphology, when considering the spheroid component. Our sample has the most robust M_{BH} determined free of assumptions on the virial factor. Thus, this is an important independent confirmation of the same underlying scaling relations between AGNs and quiescent galaxies, implying that AGNs can indeed be simply considered phases in the evolution of galaxies during which the SMBH is actively growing through accretion.

The majority of AGN host galaxies in our sample are spiral galaxies with roughly half of them having pseudo-bulges (see also e.g., Zhao et al. 2021, for a similar fraction in a sample of low-redshift PG quasars). Unlike merger-induced classical bulges, pseudo-bulges are thought to have formed through secular evolution via dissipative processes instead of galaxy mergers (e.g., Courteau et al. 1996; Korista & Goad 2004), experiencing recent or ongoing star formation (Zhao et al. 2021).

In the past, pseudo-bulges have been found to preferentially lie off the scaling relations of ellipticals and classical bulges, especially in quiescent galaxies (Kormendy & Ho 2013; see, e.g., Ríos-López et al. 2025 for a recent compilation). In the sample studied here, they do not form particular outliers in the relations, in agreement with other studies based on local type-1 AGNs (e.g., Bennert et al. 2021). It indicates that major mergers alone are not the only route to creating scaling relations, adding to predictions from purely hierarchical growth models, which posit a non-causal origin for the relations (e.g., Jahnke & Macciò 2011). Instead, AGN feedback or other mechanisms that result in fixed relative efficiencies of star formation and BH growth could play an essential role in the co-evolution of SMBHs and their hosts.

When considering the total host-galaxy luminosity, instead of just the spheroid component, we find their BHs to be residing in over-luminous hosts. In other words, M_{BH} scales more closely with spheroid luminosity than host-galaxy luminosity, in agreement with other studies (Kormendy & Ho 2013; Kormendy et al. 2011), and similar to the tighter correlations of M_{BH} and spheroid stellar velocity dispersion and stellar mass. Finding over-

luminous host galaxies of these local AGNs suggests enhanced star formation (SF) in these AGN host galaxies. However, in the literature, this topic is discussed quite controversially, with studies reporting both enhanced as well as suppressed SF in AGN host galaxies, or that SF is independent of AGN activity, with stellar mass being the underlying driving factor (see, e.g., Suh et al. 2019, for a detailed discussion).

5.3. BLR Inclination and Dependency on Other Properties

The BLR inclination derived by CARAMEL modeling is a tracer of the orientation of the central AGN engine. We here compare it with the host-galaxy disk inclination as well as properties of the AGN (BLR opening angle, accretion disk inclination and radio jet inclination).

5.3.1. BLR Inclination vs. Host Galaxy Disk Inclination

A key open question relevant to SMBH fueling is the relative orientation between the central AGN (with the accretion disk size on the order of a few light days) and its host galaxy (on the order of tens of kiloparsecs). So far, indirect tracers of the AGN inclination or position angle have been used, such as radio jets, narrow lines or dust emission, assuming the standard AGN unified model (Antonucci 1993). Results have been mixed. For example, no evidence for alignment has been found between the host galaxy stellar disks and accretion disk megamasers (with the latter generally, but not always, being well aligned with radio jets/lobes and ionization cones; Greenhill et al. 2009). Likewise, no alignment has been found between the host-galaxy major axis and the narrow-line region (NLR) traced by extended [O III] emission (which has been found to align with the radio jet axis; Schmitt et al. 2003; Fischer et al. 2013). Previous studies using radio jets as tracers of the inner AGN orientation have not found evidence for alignment with the host galaxy either (see, e.g., Kinney et al. 2000; Schmitt et al. 2002; Batty & Browne 2009, and references therein). The most recent compilation, however, compares Very Long Baseline Interferometry (VLBI) images of 5853 radio-loud AGNs (typically residing in elliptical galaxies) with Dark Energy Spectroscopic Instrument Legacy Imaging Surveys data (DESI LS), finding “a weak but significant alignment signal [...] between the parsec-scale AGN jet and the kpc projected minor axis of the optical host galaxy” (Fernández Gil et al. 2025). A prominent minor-axis alignment, depending on galaxy shape and radio power was also found by Zheng et al. (2024) for 3682 radio-loud AGNs.

For spiral galaxies, interpreting their (weak) radio emission is often not as straightforward, as the radio emission may originate from supernovae, and thus trace

the star-forming disk. Moreover, weak jets may be bent as they encounter the dense ISM in the disk. Here, we are in the unique position to compare the BLR inclination and host-galaxy disk inclination directly, for a sample of 34 spiral galaxies. For 32 AGNs with dynamical modeling of RM data, BLR size and geometry have been derived, including measurements of BLR inclination and opening angle (see Table 3, Column 12 for references). For another three AGNs, GRAVITY modeling also includes details on BLR geometry (GRAVITY Collaboration et al. 2020, 2021b, 2024). Out of these 35 galaxies, two (Mrk 110, 3C 120) were classified as ellipticals and fit with a spheroid-only component; we thus exclude them here.

For the host galaxy, we use the disk axis ratio ($q = b/a$) derived by `lenstronomy` to calculate inclination as follows

$$\cos^2 i = (q^2 - q_0^2)/(1 - q_0^2) \quad (2)$$

with $q_0 = 0.2$ (following, e.g., de Grijs 1998; Ho et al. 2011). We verified visually, that this value is indeed a reliable measure of the disk inclination, within the uncertainties (see discussion in Winkel et al. 2025). Note that in Winkel et al. (2025), $i = \arccos(b/a)$ was used, but the difference is $< 1^\circ$ for most objects and $< 3^\circ$ in all cases. Figure 2 (left panel) shows the comparison for 34 AGNs.

The parameter space is limited due to selection effects on both ends. The lowest disk inclination we derive from our fitting is $\sim 18^\circ$ ($q_{\text{disk}} = 0.95$), which is likely a consequence of constraining the disk to be more elliptical than the spheroid component during the fitting process (see (8a) in Section 4). At very high inclination, obscuration makes it harder to detect Seyferts in spiral galaxies (see, e.g., Hunt & Malkan 1999). Given that RM is based on broad-line AGNs, we would expect to preferentially select BLRs that are seen more closely to face on (for disk-like BLRs). According to the standard unified model, for type-1 AGNs, the BLR is viewed directly, at inclinations of $\sim 0\text{--}30^\circ$, while for type-2 AGNs, the BLR is obscured due to high inclination angles ($\sim 70\text{--}90^\circ$ (Antonucci 1993)). Indeed, all AGNs have BLR inclinations $< 70^\circ$, with the majority between 10 and 40° (average 29°). However, for a discussion on the complexity of the viewing angle of Seyfert types, see, e.g., Ramos Padilla et al. (2022) and references therein.

Regardless, the sample covers a large range in both BLR and host-galaxy disk inclinations ($\sim 18\text{--}70^\circ$). There is no statistically significant evidence of a correlation between BLR and host-galaxy disk inclination angles. If at all, there is an indication of a weak anti-correlation (standard Pearson correlation co-

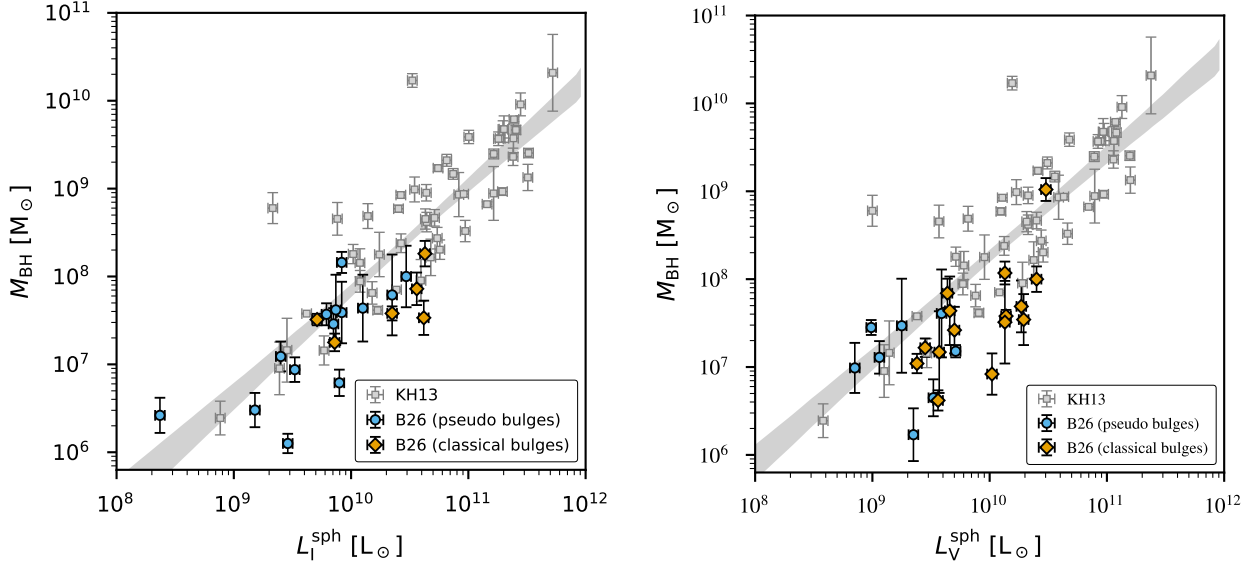


Figure 1. M_{BH} –Spheroid Luminosity Relation. In the left panel, the relation between M_{BH} and spheroid luminosity in the I -band is shown, in the right panel, the same but in the V -band. Grey data points are quiescent galaxies (ellipticals or spirals/S0 with classical bulges; Kormendy & Ho 2013); colored data points are our sample (classical bulges in yellow, pseudo-bulges in blue). The fitted relation is shown as a shaded gray stripe corresponding to the 68% (1-sigma) confidence interval of the linear regression. Since our sample consists of local AGNs with directly measured M_{BH} through dynamical modeling which is free of assumptions of the virial factor, we can show that AGNs follow the same scaling relations as those of quiescent galaxies.

Table 4. Fits to $M_{\text{BH}}-L_{\text{sph}}$ Scaling Relations

X in Relation	Sample fitted	α	β	ϵ
(6)	(7)	(8)	(9)	(10)
$L_I^{\text{sph}}/10^{11}L_{\odot}$	KH13	9.1 ± 1.2	1.05 ± 0.11	0.48 ± 0.06
	KH13+AGN	9.0 ± 1.0	1.20 ± 0.09	0.51 ± 0.05
$L_V^{\text{sph}}/10^{11}L_{\odot}$	KH13	9.5 ± 1.2	1.08 ± 0.11	0.49 ± 0.06
	KH13+AGN	9.4 ± 0.9	1.16 ± 0.09	0.52 ± 0.05

NOTE— Scaling relations of the form $\log(M_{\text{BH}}/M_{\odot}) = \alpha + \beta \log X$. All fits calculated in this paper. Col. (1): X used in the scaling relation. Col. (2): Sample for which the $M_{\text{BH}}-L_{\text{sph}}$ relation was fitted. KH13 is the comparison sample of 51 quiescent galaxies (Kormendy & Ho 2013). “AGN” refers to sample of local RM AGNs in this paper. Col. (3): Best-fit intercept of the $M_{\text{BH}}-L_{\text{sph}}$ relation. Col. (4): Best-fit slope. Col. (5): Best-fit intrinsic scatter.

efficient of -0.16). A similar conclusion has previously been reached by [Du et al. \(2025\)](#), based on a much smaller sample of 8 objects (which are also included in this study), and calculating galaxy inclination angles from 2MASS K_s -band images.

Our result is seemingly contradictory to the recent findings of radio jets being aligned with the host-galaxy minor axis ([Zheng et al. 2024](#); [Fernández Gil et al. 2025](#)). One reason for the different results may be the different host galaxy morphologies. The radio-loud AGNs in these studies are known to be typically hosted by elliptical galaxies. Our sample, however, as well as megamaser host galaxies are spiral galaxies. Another study of 18 disk galaxies with extended double-lobed radio structures also found a misalignment ([Wu et al. 2022](#)). While high-resolution simulations show that misalignments between AGNs and host galaxies are expected for both galaxy major mergers as well as for instabilities in isolated disks ([Hopkins et al. 2012](#)), the observed differences in inner AGN (mis-)alignment with outer host galaxy have been interpreted differently by [Fernández Gil et al. \(2025\)](#). They argue that spiral galaxies, predominantly formed through secular evolution and gas accretion from cosmic filaments, fuel SMBHs through minor mergers and cosmic gas accretion which occur isotropically, and thus result in a random orientation between accretion disk and host-galaxy disk. Major mergers, on the other hand, form a spheroid elongated in the direction of the incoming companion, with tidal debris fueling the SMBH along the same direction. Our findings are in agreement with this interpretation.

5.3.2. BLR Inclination vs. BLR Opening Angle

While the host-galaxy disk inclination angle can be relatively robustly determined for these well-resolved, nearby galaxies imaged by HST, we here address the question of possible degeneracies in the CARAMEL model. BLR inclination is only one of the parameters used in CARAMEL to describe BLR geometry; another important related one is the BLR opening angle, which changes the geometry from a thin disk to a sphere. In Figure 2 (right panel), we show the distributions of BLR inclination angles vs. BLR opening angles. Here, the Pearson correlation coefficient is 0.71, indicating that both parameters are correlated. LinMix gives a best-fit linear regression of $i_{\text{BLR}} = (2 \pm 5)^\circ + (0.8 \pm 0.2) o_{\text{BLR}}$ with an intrinsic scatter of $(5 \pm 2)^\circ$. The relation between BLR inclination and opening angle was noted and discussed already in [Grier et al. \(2017\)](#), based on a much smaller sample. To understand this relation, it is important to remember what these parameters mean. The smaller the inclination angle, the more face-on the BLR is seen;

the larger, the more edge-on. The smaller the opening angle, the more disk-like is the BLR; the larger the more spherical (see, e.g., Figure 9 in [Pancoast et al. 2014](#)). For a given inclination angle, if the opening angle becomes too small (i.e., disk-shaped), the emission line profile will show double peaked lines. However, double-peaked emission lines are not seen in this sample, so the opening angle cannot be much smaller than the inclination angle.

On the other hand, as the opening angle becomes larger than the inclination angle, the transfer function becomes spread out in both time lag and wavelength space. As [Grier et al. \(2017\)](#) summarize: “If the data prefer a more compact transfer function, it will thus force the opening angle to be as small as possible while still producing a single-peaked line profile.” So the correlation between BLR inclination and opening angle is not driven by a degeneracy in the CARAMEL model, but rather by the physical requirements of the observed data (transfer function and line profiles). [Grier et al. \(2017\)](#) perform tests varying inclination and opening angles, suggesting that the inclination angle is more robustly determined than the opening angle. Note that, naturally, the uncertainties on the derived inclination angles increase towards more spherical BLRs (i.e., large opening angles), as the inclination cannot be robustly determined for a spherical shape.

5.3.3. BLR Inclination vs. Accretion Disk and Jet Inclination

Further support for the robustness of the BLR inclination angle determined by CARAMEL comes from two independent approaches: (1) using X-ray data to estimate the accretion-disk inclination; (2) using radio data to determine radio jet inclination.

(1) For eight AGNs (also included in our sample), [Du et al. \(2025\)](#) derive the accretion disk inclination angle based on X-ray broadband reflection spectroscopy. When compared to the BLR inclination angle (as derived from CARAMEL), they report a nearly linear relation (even though with marginal significance, given their small sample). The relation suggests that the rotational axes of BLR and accretion disk are aligned, supporting a physical connection between accretion disk and BLR, e.g., through disk winds ([Peterson 2006](#); [Czerny & Hrynowicz 2011](#)). Taking an Occam’s Razor approach, we interpret the nearly linear relation between BLR and accretion disk inclinations as evidence for the robustness of the the BLR inclination angles determined by CARAMEL.

(2) While the majority of AGNs in the CARAMEL sample are radio-quiet, there are three objects for which the radio jet inclination axis has been determined. Two

AGNs are radio-loud (3C 120 and 3C 273) and one is a so-called radio-intermediate quasar (Mrk1501, also known as IIIZw 2 or PG 0007+106; thought to be relativistically boosted counterparts of radio-quiet quasars; e.g., Falcke et al. 1996). For 3C 120, the radio jet inclination $i_{\text{radio jet}} = 16 \pm 2^\circ$ (Agudo et al. 2012) is, within the uncertainties, identical to the BLR inclination $i_{\text{BLR}} = 17.6_{-3.3}^{+5.4}{}^\circ$ (CARMEL; Grier et al. 2017). The host is an elliptical galaxy with signs of interactions (one-armed tidal tail). For 3C 273, the radio jet inclination $i_{\text{radio jet}} = 5.5 \pm 1.7^\circ$ (Meyer et al. 2016) also agrees well with the BLR inclination $i_{\text{BLR}} = 5 \pm 1^\circ$ (GRAVITY/SARM; Li et al. 2022). This radio-loud AGN is hosted by an elliptical galaxy that was not included in the HST decomposition presented here, due to an insufficient PSF fit (however, see Bentz et al. 2009, for a decomposition). Lastly, for Mrk 1501, $i_{\text{radio jet}} = 22.1^\circ$ (Liodakis et al. 2018) compares to $i_{\text{BLR}} = 20.5_{-5.7}^{+5}{}^\circ$ (CARMEL; Grier et al. 2017), with a host-galaxy disk inclination of 52° . In all three cases, the radio jet inclination agrees well with the BLR inclination derived by the dynamical modeling.

The relation between BLR inclination and either (1) accretion disk inclination or (2) radio jet inclination is shown in Fig. 3. The Pearson correlation coefficient is 0.9, and LinMix gives a best-fit linear regression of $i_{\text{BLR}} = (-6 \pm 25)^\circ + (1.4 \pm 1) i_{\text{accretion disk/jet}}$ with an intrinsic scatter of $(5 \pm 5)^\circ$.

The close agreement between the BLR and accretion disk or jet inclination angles is remarkable, given the independent derivations, at different wavelengths and scales. These findings support the standard view of inner AGN structure, with the BLR, accretion disk and jet aligned. They are also further and independent evidence that the BLR inclination angle derived by CARMEL can be considered robust.

6. SUMMARY

In this paper, HST images are analyzed of a sample of 44 type-1 AGNs with the most robust BH mass measurements in the local universe. Using surface-brightness profile fitting with state-of-the-art programs, we derive AGN luminosity, as well as radii and luminosities of spheroid, disk and bar (if present). The spheroid and galaxy effective radii were used in Winkel et al. (2025) to measure stellar velocity dispersion from integral-field spectroscopy. We demonstrated – for the first time – that AGNs follow the same $M_{\text{BH}}-\sigma_*$ and $M_{\text{BH}}-M_{\text{sph,dyn}}$ relations as quiescent galaxies. Here, we expand the study to other host-galaxy properties. Our results can be summarized as follows.

- The majority of AGNs in our sample are hosted by spiral or S0 galaxies (91%), with roughly half having a prominent bar. Also roughly half were determined to host pseudo-bulges. Major mergers are rare (5%), with another $\sim 15\text{--}20\%$ showing signs of interactions or minor mergers.
- Within the uncertainties, the $M_{\text{BH}}-L_{\text{sph}}$ relation matches that of quiescent galaxies. Combined with the results in our earlier paper, for moderate luminosity AGNs in the local universe, all three scaling relations $M_{\text{BH}}-\sigma_*$, $M_{\text{BH}}-M_{\text{sph,dyn}}$ and $M_{\text{BH}}-L_{\text{sph}}$ match those of quiescent galaxies. Pseudo-bulges are not outliers.
- For our sample of spiral galaxies, the BLR inclination and host-galaxy disk inclination angles are uncorrelated. This is contrary to a recent studies of radio jets in elliptical galaxies for which an alignment between parsec-scale AGN jet and kpc projected minor axis of the optical host galaxy was found. The difference is likely due to the different nature and formation of their host galaxies.
- BLR inclination and opening angle are positively related, driven by the need of the model to account for the single-peaked emission lines observed in the sample.
- For three radio-loud AGNs in the sample, the radio jet inclination agrees well with the BLR inclination. For eight AGNs, the same is true between the accretion disk inclination and BLR inclination. These findings not only provide independent evidence that the derived BLR inclination angle is robust, they also support the standard view of the inner AGN structure, with BLR, accretion disk and jet aligned.

Our sample has the most accurate M_{BH} measurements beyond the local universe and provides a fundamental local benchmark for studies of the evolution of massive black holes and their host galaxies across cosmic time.

ACKNOWLEDGEMENTS

All HST data used in this paper can be found in MAST: doi:10.17909/2g2m-rx22. We thank the anonymous referee for their thoughtful comments that helped to improve the paper. VNB thanks Eric Emsellem and Andrea Merloni for fruitful discussions, and Victoria Bollo and Pranav Kukreti for their help with the radio observations. VNB gratefully acknowledges support through the European Southern Observatory (ESO) Scientific

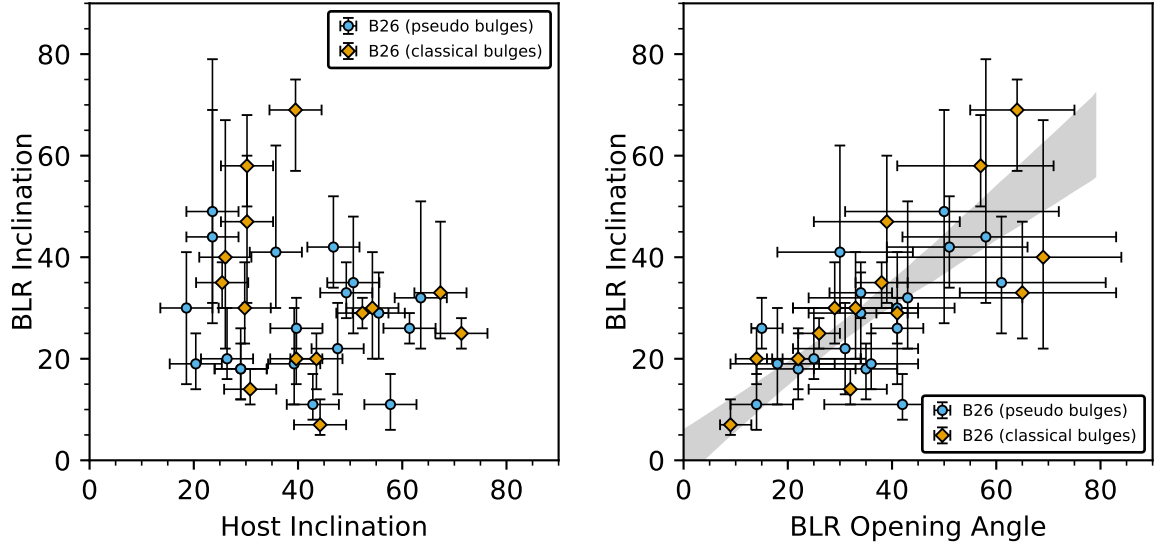


Figure 2. *Left:* BLR Inclination vs. Host Inclination. Comparison between inclination of the BLR, based on CARAMEL and GRAVITY modeling, and host-galaxy disk inclination, for our sample of 34 RM AGNs (classical bulges in yellow, pseudo-bulges in blue). There is no correlation between the inclination of the central AGN and the large-scale host-galaxy disk; if at all, there is an indication of a weak anti-correlation (Pearson correlation coefficient of -0.16). *Right:* BLR Inclination vs. BLR Opening Angle. Similar to the left panel, but now comparing inclination and opening angle of the BLR, based on CARAMEL and GRAVITY modeling. Both parameters are correlated (Pearson correlation coefficient of 0.71). The fitted relation is shown as a shaded gray stripe corresponding to the 68% (1-sigma) confidence interval of the linear regression. The correlation is driven by the absence of double-peaked lines in the sample. In other words, in modeling the data, the opening angle of the BLR cannot be much smaller than the inclination angle, while still reproducing the observed single-peaked lines.

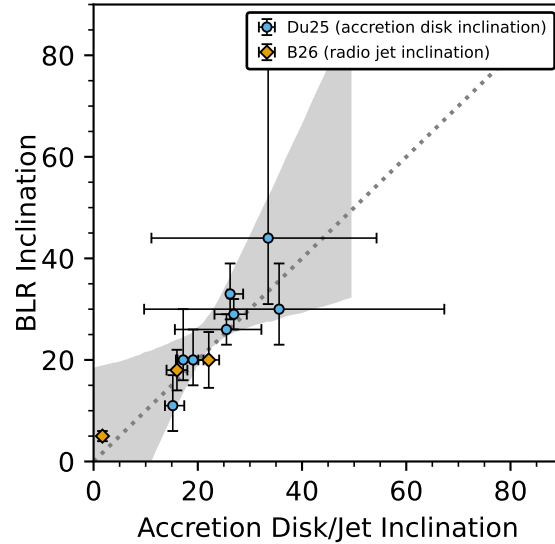


Figure 3. BLR Inclination vs. Accretion Disk/Jet Inclination. Comparison between inclination of the BLR, based on CARAMEL modeling and accretion disk inclination (Du et al. 2025) or radio-jet inclination (compiled in this paper). Both parameters are correlated (Pearson correlation coefficient of 0.9). The fitted relation is shown as a shaded gray stripe corresponding to the 68% (1-sigma) confidence interval of the linear regression. (The 1:1 dotted line is shown for comparison only.)

Visitor Program. This work is based on observations with the NASA/ESA Hubble Space Telescope obtained from the Data Archive at the Space Telescope Science Institute, which is operated by the Association of Universities for Research in Astronomy, Incorporated, under NASA contract NAS5-26555. Financial support for Program number HST-GO 17103 (PI Bennert) and HST-AR 17063 (PI Bennert) was provided through a grant from the STScI under NASA contract NAS5-26555. NW was supported by the German Science Foundation (DFG) under grant number HU1777/3-1. MK was supported by the National Research Foundation of Korea (NRF) grant funded by the Korean government

(MSIT) (No. RS-2024-00347548). ChatGPT (version 4.0 and 5.0) was used for occasional minor help with Python coding (finding bugs, help with plotting, etc.) and minor text edits (typos and grammar).

Facilities: Keck:II (KCWI), VLT:Yepun (MUSE), VLT:Melipal (VIMOS), HST (ACS, WFCP2, WFC3)

Software: `AstroDrizzle` (Fruchter et al. 2010), `Astropy` (Astropy Collaboration et al. 2013, 2018), `GALFIT` (Peng et al. 2002), `galight` (Ding et al. 2020), `LA-Cosmic` (van Dokkum 2001), `Lenstronomy` (Birrer & Amara 2018), `LinMix` (Kelly 2007), `psfr` (Birrer et al. 2019), `SciPy` (Virtanen et al. 2020)

REFERENCES

Agudo, I., Gómez, J. L., Casadio, C., Cawthorne, T. V., & Roca-Sogorb, M. 2012, ApJ, 752, 92, doi: [10.1088/0004-637X/752/2/92](https://doi.org/10.1088/0004-637X/752/2/92)

Antonucci, R. 1993, ARAA, 31, 473, doi: [10.1146/annurev.aa.31.090193.002353](https://doi.org/10.1146/annurev.aa.31.090193.002353)

Astropy Collaboration, Robitaille, T. P., Tollerud, E. J., et al. 2013, A&A, 558, A33, doi: [10.1051/0004-6361/201322068](https://doi.org/10.1051/0004-6361/201322068)

Astropy Collaboration, Price-Whelan, A. M., Sipőcz, B. M., et al. 2018, AJ, 156, 123, doi: [10.3847/1538-3881/aabc4f](https://doi.org/10.3847/1538-3881/aabc4f)

Battye, R. A., & Browne, I. W. A. 2009, MNRAS, 399, 1888, doi: [10.1111/j.1365-2966.2009.15429.x](https://doi.org/10.1111/j.1365-2966.2009.15429.x)

Bennert, N., Canalizo, G., Jungwiert, B., et al. 2008, ApJ, 677, 846, doi: [10.1086/529068](https://doi.org/10.1086/529068)

Bennert, V. N., Treu, T., Woo, J.-H., et al. 2010, ApJ, 708, 1507, doi: [10.1088/0004-637X/708/2/1507](https://doi.org/10.1088/0004-637X/708/2/1507)

Bennert, V. N., Treu, T., Auger, M. W., et al. 2015, ApJ, 809, 20, doi: [10.1088/0004-637X/809/1/20](https://doi.org/10.1088/0004-637X/809/1/20)

Bennert, V. N., Treu, T., Ding, X., et al. 2021, ApJ, 921, 36, doi: [10.3847/1538-4357/ac151a](https://doi.org/10.3847/1538-4357/ac151a)

Bentz, M. C., & Manne-Nicholas, E. 2018, ApJ, 864, 146, doi: [10.3847/1538-4357/aad808](https://doi.org/10.3847/1538-4357/aad808)

Bentz, M. C., Markham, M., Rosborough, S., et al. 2023a, ApJ, 959, 25, doi: [10.3847/1538-4357/ad08b8](https://doi.org/10.3847/1538-4357/ad08b8)

Bentz, M. C., Onken, C. A., Street, R., & Valluri, M. 2023b, ApJ, 944, 29, doi: [10.3847/1538-4357/acab62](https://doi.org/10.3847/1538-4357/acab62)

Bentz, M. C., Peterson, B. M., Netzer, H., Pogge, R. W., & Vestergaard, M. 2009, ApJ, 697, 160, doi: [10.1088/0004-637X/697/1/160](https://doi.org/10.1088/0004-637X/697/1/160)

Bentz, M. C., Peterson, B. M., Pogge, R. W., Vestergaard, M., & Onken, C. A. 2006, ApJ, 644, 133, doi: [10.1086/503537](https://doi.org/10.1086/503537)

Bentz, M. C., Street, R., Onken, C. A., & Valluri, M. 2021, ApJ, 906, 50, doi: [10.3847/1538-4357/abcc4](https://doi.org/10.3847/1538-4357/abcc4)

Bentz, M. C., Williams, P. R., & Treu, T. 2022, ApJ, 934, 168, doi: [10.3847/1538-4357/ac7c0a](https://doi.org/10.3847/1538-4357/ac7c0a)

Bentz, M. C., Denney, K. D., Grier, C. J., et al. 2013, ApJ, 767, 149, doi: [10.1088/0004-637X/767/2/149](https://doi.org/10.1088/0004-637X/767/2/149)

Birrer, S., & Amara, A. 2018, Physics of the Dark Universe, 22, 189, doi: [10.1016/j.dark.2018.11.002](https://doi.org/10.1016/j.dark.2018.11.002)

Birrer, S., Treu, T., Rusu, C. E., et al. 2019, MNRAS, 484, 4726, doi: [10.1093/mnras/stz200](https://doi.org/10.1093/mnras/stz200)

Birrer, S., Shajib, A., Gilman, D., et al. 2021, The Journal of Open Source Software, 6, 3283, doi: [10.21105/joss.03283](https://doi.org/10.21105/joss.03283)

Brewer, B. J., Treu, T., Pancoast, A., et al. 2011, ApJL, 733, L33, doi: [10.1088/2041-8205/733/2/L33](https://doi.org/10.1088/2041-8205/733/2/L33)

Canalizo, G., Bennert, N., Jungwiert, B., et al. 2007, ApJ, 669, 801, doi: [10.1086/521721](https://doi.org/10.1086/521721)

Courteau, S., de Jong, R. S., & Broeils, A. H. 1996, ApJL, 457, L73, doi: [10.1086/309906](https://doi.org/10.1086/309906)

Czerny, B., & Hryniewicz, K. 2011, A&A, 525, L8, doi: [10.1051/0004-6361/201016025](https://doi.org/10.1051/0004-6361/201016025)

de Grijs, R. 1998, MNRAS, 299, 595, doi: [10.1046/j.1365-8711.1998.01896.x](https://doi.org/10.1046/j.1365-8711.1998.01896.x)

De Rosa, G., Fausnaugh, M. M., Grier, C. J., et al. 2018, ApJ, 866, 133, doi: [10.3847/1538-4357/aadd11](https://doi.org/10.3847/1538-4357/aadd11)

Debattista, V. P., Kazantzidis, S., & van den Bosch, F. C. 2013, ApJ, 765, 23, doi: [10.1088/0004-637X/765/1/23](https://doi.org/10.1088/0004-637X/765/1/23)

Di Matteo, T., Springel, V., & Hernquist, L. 2005, Nature, 433, 604, doi: [10.1038/nature03335](https://doi.org/10.1038/nature03335)

Ding, X., Silverman, J., Treu, T., et al. 2020, ApJ, 888, 37, doi: [10.3847/1538-4357/ab5b90](https://doi.org/10.3847/1538-4357/ab5b90)

Ding, X., Treu, T., Birrer, S., et al. 2021, MNRAS, 501, 269, doi: [10.1093/mnras/staa2992](https://doi.org/10.1093/mnras/staa2992)

Du, P., Hu, C., Lu, K.-X., et al. 2015, ApJ, 806, 22, doi: [10.1088/0004-637X/806/1/22](https://doi.org/10.1088/0004-637X/806/1/22)

Du, R., Ho, L. C., Ding, Y., & Li, R. 2025, *ApJ*, 988, 3, doi: [10.3847/1538-4357/addec8](https://doi.org/10.3847/1538-4357/addec8)

Fabian, A. C. 2012, *ARA&A*, 50, 455, doi: [10.1146/annurev-astro-081811-125521](https://doi.org/10.1146/annurev-astro-081811-125521)

Falcke, H., Sherwood, W., & Patnaik, A. R. 1996, *ApJ*, 471, 106, doi: [10.1086/177956](https://doi.org/10.1086/177956)

Fausnaugh, M. M., Grier, C. J., Bentz, M. C., et al. 2017, *ApJ*, 840, 97, doi: [10.3847/1538-4357/aa6d52](https://doi.org/10.3847/1538-4357/aa6d52)

Fernández Gil, D., Hodgson, J. A., L’Huillier, B., et al. 2025, *Nature Astronomy*, 9, 302, doi: [10.1038/s41550-024-02407-4](https://doi.org/10.1038/s41550-024-02407-4)

Ferrarese, L., & Ford, H. 2005, *SSRv*, 116, 523, doi: [10.1007/s11214-005-3947-6](https://doi.org/10.1007/s11214-005-3947-6)

Ferrarese, L., & Merritt, D. 2000, *ApJL*, 539, L9, doi: [10.1086/312838](https://doi.org/10.1086/312838)

Fischer, T. C., Crenshaw, D. M., Kraemer, S. B., & Schmitt, H. R. 2013, *ApJS*, 209, 1, doi: [10.1088/0067-0049/209/1/1](https://doi.org/10.1088/0067-0049/209/1/1)

Fruchter, A. S., Hack, W., Dencheva, N., Droettboom, M., & Greenfield, P. 2010, in 2010 Space Telescope Science Institute Calibration Workshop, 382–387

Gebhardt, K., Bender, R., Bower, G., et al. 2000, *ApJL*, 539, L13, doi: [10.1086/312840](https://doi.org/10.1086/312840)

Graham, A. W. 2016, in *Astrophysics and Space Science Library*, Vol. 418, Galactic Bulges, ed. E. Laurikainen, R. Peletier, & D. Gadotti, 263, doi: [10.1007/978-3-319-19378-6_11](https://doi.org/10.1007/978-3-319-19378-6_11)

GRAVITY Collaboration, Sturm, E., Dexter, J., et al. 2018, *Nature*, 563, 657, doi: [10.1038/s41586-018-0731-9](https://doi.org/10.1038/s41586-018-0731-9)

GRAVITY Collaboration, Amorim, A., Bauböck, M., et al. 2020, *A&A*, 643, A154, doi: [10.1051/0004-6361/202039067](https://doi.org/10.1051/0004-6361/202039067)

—. 2021a, *A&A*, 648, A117, doi: [10.1051/0004-6361/202040061](https://doi.org/10.1051/0004-6361/202040061)

—. 2021b, *A&A*, 654, A85, doi: [10.1051/0004-6361/202141426](https://doi.org/10.1051/0004-6361/202141426)

GRAVITY Collaboration, Amorim, A., Bourdarot, G., et al. 2024, *A&A*, 684, A167, doi: [10.1051/0004-6361/202348167](https://doi.org/10.1051/0004-6361/202348167)

Greene, J. E., Labbe, I., Goulding, A. D., et al. 2024, *ApJ*, 964, 39, doi: [10.3847/1538-4357/ad1e5f](https://doi.org/10.3847/1538-4357/ad1e5f)

Greenhill, L. J., Kondratko, P. T., Moran, J. M., & Tilak, A. 2009, *ApJ*, 707, 787, doi: [10.1088/0004-637X/707/1/787](https://doi.org/10.1088/0004-637X/707/1/787)

Grier, C. J., Pancoast, A., Barth, A. J., et al. 2017, *ApJ*, 849, 146, doi: [10.3847/1538-4357/aa901b](https://doi.org/10.3847/1538-4357/aa901b)

Grogin, N. A., Lim, P. L., Maybhate, A., Hook, R. N., & Loose, M. 2010, in *Hubble after SM4. Preparing JWST*, ed. S. Deustua & C. Oliveira, 54

Grogin, N. A., Lim, P. L., Maybhate, A., Hook, R. N., & Loose, M. 2011, *Post-SM4 ACS/WFC Bias Striping: Characterization and Mitigation, Instrument Science Report ACS 2011-05*, 25 pages

Harris, W. E. 2018, *AJ*, 156, 296, doi: [10.3847/1538-3881/aaedb8](https://doi.org/10.3847/1538-3881/aaedb8)

Hartmann, M., Debattista, V. P., Cole, D. R., et al. 2014, *MNRAS*, 441, 1243, doi: [10.1093/mnras/stu627](https://doi.org/10.1093/mnras/stu627)

Heckman, T. M., & Best, P. N. 2014, *ARAA*, 52, 589, doi: [10.1146/annurev-astro-081913-035722](https://doi.org/10.1146/annurev-astro-081913-035722)

Ho, L. C., Li, Z.-Y., Barth, A. J., Seigar, M. S., & Peng, C. Y. 2011, *ApJS*, 197, 21, doi: [10.1088/0067-0049/197/2/21](https://doi.org/10.1088/0067-0049/197/2/21)

Hopkins, P. F., Hernquist, L., Hayward, C. C., & Narayanan, D. 2012, *MNRAS*, 425, 1121, doi: [10.1111/j.1365-2966.2012.21449.x](https://doi.org/10.1111/j.1365-2966.2012.21449.x)

Hopkins, P. F., Torrey, P., Faucher-Giguère, C.-A., Quataert, E., & Murray, N. 2016, *MNRAS*, 458, 816, doi: [10.1093/mnras/stw289](https://doi.org/10.1093/mnras/stw289)

Hu, C., Li, S.-S., Yang, S., et al. 2021, *ApJS*, 253, 20, doi: [10.3847/1538-4365/abd774](https://doi.org/10.3847/1538-4365/abd774)

Hunt, L. K., & Malkan, M. A. 1999, *ApJ*, 516, 660, doi: [10.1086/307150](https://doi.org/10.1086/307150)

Husemann, B., Singha, M., Scharwächter, J., et al. 2022, *A&A*, 659, A124, doi: [10.1051/0004-6361/202141312](https://doi.org/10.1051/0004-6361/202141312)

Jahnke, K., & Macciò, A. V. 2011, *ApJ*, 734, 92, doi: [10.1088/0004-637X/734/2/92](https://doi.org/10.1088/0004-637X/734/2/92)

Kaspi, S., Smith, P. S., Netzer, H., et al. 2000, *ApJ*, 533, 631, doi: [10.1086/308704](https://doi.org/10.1086/308704)

Kelly, B. C. 2007, *ApJ*, 665, 1489, doi: [10.1086/519947](https://doi.org/10.1086/519947)

Kim, M., Barth, A. J., Ho, L. C., & Son, S. 2021, *ApJS*, 256, 40, doi: [10.3847/1538-4365/ac133e](https://doi.org/10.3847/1538-4365/ac133e)

Kim, M., Ho, L. C., Peng, C. Y., Barth, A. J., & Im, M. 2017, *ApJS*, 232, 21, doi: [10.3847/1538-4365/aa8a75](https://doi.org/10.3847/1538-4365/aa8a75)

Kinney, A. L., Calzetti, D., Bohlin, R. C., et al. 1996, *ApJ*, 467, 38, doi: [10.1086/177583](https://doi.org/10.1086/177583)

Kinney, A. L., Schmitt, H. R., Clarke, C. J., et al. 2000, *ApJ*, 537, 152, doi: [10.1086/309016](https://doi.org/10.1086/309016)

Kocevski, D. D., Faber, S. M., Mozena, M., et al. 2012, *ApJ*, 744, 148, doi: [10.1088/0004-637X/744/2/148](https://doi.org/10.1088/0004-637X/744/2/148)

Korista, K. T., & Goad, M. R. 2004, *ApJ*, 606, 749, doi: [10.1086/383193](https://doi.org/10.1086/383193)

Kormendy, J., Bender, R., & Cornell, M. E. 2011, *Nature*, 469, 374, doi: [10.1038/nature09694](https://doi.org/10.1038/nature09694)

Kormendy, J., & Ho, L. C. 2013, *ARA&A*, 51, 511, doi: [10.1146/annurev-astro-082708-101811](https://doi.org/10.1146/annurev-astro-082708-101811)

Li, Y.-R., Wang, J.-M., Ho, L. C., Du, P., & Bai, J.-M. 2013, *ApJ*, 779, 110, doi: [10.1088/0004-637X/779/2/110](https://doi.org/10.1088/0004-637X/779/2/110)

Li, Y.-R., Wang, J.-M., Songsheng, Y.-Y., et al. 2022, *ApJ*, 927, 58, doi: [10.3847/1538-4357/ac4bcb](https://doi.org/10.3847/1538-4357/ac4bcb)

Li, Y.-R., Songsheng, Y.-Y., Qiu, J., et al. 2018, *ApJ*, 869, 137, doi: [10.3847/1538-4357/aae6b](https://doi.org/10.3847/1538-4357/aae6b)

Liodakis, I., Hovatta, T., Huppenkothen, D., et al. 2018, *ApJ*, 866, 137, doi: [10.3847/1538-4357/aae2b7](https://doi.org/10.3847/1538-4357/aae2b7)

Lu, K.-X., Wang, J.-G., Zhang, Z.-X., et al. 2021, *ApJ*, 918, 50, doi: [10.3847/1538-4357/ac0c78](https://doi.org/10.3847/1538-4357/ac0c78)

Magorrian, J., Tremaine, S., Richstone, D., et al. 1998, *AJ*, 115, 2285, doi: [10.1086/300353](https://doi.org/10.1086/300353)

Malkan, M. A., Gorjian, V., & Tam, R. 1998, *ApJS*, 117, 25, doi: [10.1086/313110](https://doi.org/10.1086/313110)

Mandal, A. K., Schramm, M., Rakshit, S., et al. 2021, *MNRAS*, 508, 5296, doi: [10.1093/mnras/stab2909](https://doi.org/10.1093/mnras/stab2909)

Marian, V., Jahnke, K., Mechtley, M., et al. 2019, *ApJ*, 882, 141, doi: [10.3847/1538-4357/ab385b](https://doi.org/10.3847/1538-4357/ab385b)

Meyer, E. T., Sparks, W. B., Georganopoulos, M., et al. 2016, *ApJ*, 818, 195, doi: [10.3847/0004-637X/818/2/195](https://doi.org/10.3847/0004-637X/818/2/195)

Morganti, R. 2017, *Frontiers in Astronomy and Space Sciences*, 4, 42, doi: [10.3389/fspas.2017.00042](https://doi.org/10.3389/fspas.2017.00042)

Mortlock, D. J., Warren, S. J., Venemans, B. P., et al. 2011, *Nat*, 474, 616, doi: [10.1038/nature10159](https://doi.org/10.1038/nature10159)

Onken, C. A., Ferrarese, L., Merritt, D., et al. 2004, *ApJ*, 615, 645, doi: [10.1086/424655](https://doi.org/10.1086/424655)

Pacucci, F., & Loeb, A. 2024, *ApJ*, 964, 154, doi: [10.3847/1538-4357/ad3044](https://doi.org/10.3847/1538-4357/ad3044)

Pagul, A., & Rivera, I. 2024, in *WFC3 Data Handbook v. 6*, Vol. 6, 6

Pancoast, A., Brewer, B. J., & Treu, T. 2011, *ApJ*, 730, 139, doi: [10.1088/0004-637X/730/2/139](https://doi.org/10.1088/0004-637X/730/2/139)

Pancoast, A., Brewer, B. J., Treu, T., et al. 2014, *MNRAS*, 445, 3073, doi: [10.1093/mnras/stu1419](https://doi.org/10.1093/mnras/stu1419)

Pancoast, A., Barth, A. J., Horne, K., et al. 2018, *ApJ*, 856, 108, doi: [10.3847/1538-4357/aab3c6](https://doi.org/10.3847/1538-4357/aab3c6)

Park, D., Kelly, B. C., Woo, J.-H., & Treu, T. 2012, *ApJS*, 203, 6, doi: [10.1088/0067-0049/203/1/6](https://doi.org/10.1088/0067-0049/203/1/6)

Parker, M. L., Schartel, N., Komossa, S., et al. 2014, *MNRAS*, 445, 1039, doi: [10.1093/mnras/stu1818](https://doi.org/10.1093/mnras/stu1818)

Peng, C. Y. 2007, *ApJ*, 671, 1098, doi: [10.1086/522774](https://doi.org/10.1086/522774)

Peng, C. Y., Ho, L. C., Impey, C. D., & Rix, H.-W. 2002, *AJ*, 124, 266, doi: [10.1086/340952](https://doi.org/10.1086/340952)

Peterson, B. M. 2006, in *Physics of Active Galactic Nuclei at all Scales*, ed. D. Alloin, Vol. 693, 77, doi: [10.1007/3-540-34621-X_3](https://doi.org/10.1007/3-540-34621-X_3)

Planck Collaboration, Ade, P. A. R., Aghanim, N., et al. 2016, *A&A*, 594, A13, doi: [10.1051/0004-6361/201525830](https://doi.org/10.1051/0004-6361/201525830)

Rakshit, S., Stalin, C. S., & Kotilainen, J. 2020, *ApJS*, 249, 17, doi: [10.3847/1538-4365/ab99c5](https://doi.org/10.3847/1538-4365/ab99c5)

Ramos Padilla, A. F., Wang, L., Małek, K., Efstathiou, A., & Yang, G. 2022, *MNRAS*, 510, 687, doi: [10.1093/mnras/stab3486](https://doi.org/10.1093/mnras/stab3486)

Remigio, R. P., U, V., Barth, A. J., et al. 2025, *ApJ*, 992, 42, doi: [10.3847/1538-4357/adfe5d](https://doi.org/10.3847/1538-4357/adfe5d)

Ríos-López, E., López-Cruz, O., Añorve, C., et al. 2025, *MNRAS*, 539, 2583, doi: [10.1093/mnras/staf606](https://doi.org/10.1093/mnras/staf606)

Schawinski, K., Simmons, B. D., Urry, C. M., Treister, E., & Glikman, E. 2012, *MNRAS*, 425, L61, doi: [10.1111/j.1745-3933.2012.01302.x](https://doi.org/10.1111/j.1745-3933.2012.01302.x)

Schlafly, E. F., & Finkbeiner, D. P. 2011, *ApJ*, 737, 103, doi: [10.1088/0004-637X/737/2/103](https://doi.org/10.1088/0004-637X/737/2/103)

Schmitt, H. R., Donley, J. L., Antonucci, R. R. J., et al. 2003, *ApJ*, 597, 768, doi: [10.1086/381224](https://doi.org/10.1086/381224)

Schmitt, H. R., Pringle, J. E., Clarke, C. J., & Kinney, A. L. 2002, *ApJ*, 575, 150, doi: [10.1086/341211](https://doi.org/10.1086/341211)

Shajib, A. J., Birrer, S., Treu, T., et al. 2019, *MNRAS*, 483, 5649, doi: [10.1093/mnras/sty3397](https://doi.org/10.1093/mnras/sty3397)

—. 2020, *MNRAS*, 494, 6072, doi: [10.1093/mnras/staa828](https://doi.org/10.1093/mnras/staa828)

Shen, Y., Richards, G. T., Strauss, M. A., et al. 2011, *ApJS*, 194, 45, doi: [10.1088/0067-0049/194/2/45](https://doi.org/10.1088/0067-0049/194/2/45)

Stone, Z., Shen, Y., Anderson, S. F., et al. 2025, *ApJ*, 991, 218, doi: [10.3847/1538-4357/adfd4c](https://doi.org/10.3847/1538-4357/adfd4c)

Suh, H., Civano, F., Hasinger, G., et al. 2019, *ApJ*, 872, 168, doi: [10.3847/1538-4357/ab01fb](https://doi.org/10.3847/1538-4357/ab01fb)

Treu, T., Malkan, M. A., & Blandford, R. D. 2004, *ApJL*, 615, L97, doi: [10.1086/426437](https://doi.org/10.1086/426437)

U, V., Barth, A. J., Vogler, H. A., et al. 2022, *ApJ*, 925, 52, doi: [10.3847/1538-4357/ac3d26](https://doi.org/10.3847/1538-4357/ac3d26)

van Dokkum, P. G. 2001, *PASP*, 113, 1420, doi: [10.1086/323894](https://doi.org/10.1086/323894)

Vestergaard, M. 2002, *ApJ*, 571, 733, doi: [10.1086/340045](https://doi.org/10.1086/340045)

Villafañá, L., Williams, P. R., Treu, T., et al. 2022, *ApJ*, 930, 52, doi: [10.3847/1538-4357/ac6171](https://doi.org/10.3847/1538-4357/ac6171)

—. 2023, *ApJ*, 948, 95, doi: [10.3847/1538-4357/accc84](https://doi.org/10.3847/1538-4357/accc84)

Virtanen, P., Gommers, R., Oliphant, T. E., et al. 2020, *Nature Methods*, 17, 261, doi: [10.1038/s41592-019-0686-2](https://doi.org/10.1038/s41592-019-0686-2)

Wandel, A., Peterson, B. M., & Malkan, M. A. 1999, *ApJ*, 526, 579, doi: [10.1086/308017](https://doi.org/10.1086/308017)

Williams, P. R., Pancoast, A., Treu, T., et al. 2018, *ApJ*, 866, 75, doi: [10.3847/1538-4357/aae086](https://doi.org/10.3847/1538-4357/aae086)

—. 2020, *ApJ*, 902, 74, doi: [10.3847/1538-4357/abbad7](https://doi.org/10.3847/1538-4357/abbad7)

Willott, C. J., Albert, L., Arzoumanian, D., et al. 2010, *AJ*, 140, 546, doi: [10.1088/0004-6256/140/2/546](https://doi.org/10.1088/0004-6256/140/2/546)

Winkel, N., Bennert, V. N., Remigio, R. P., et al. 2025, *ApJ*, 978, 115, doi: [10.3847/1538-4357/ad9272](https://doi.org/10.3847/1538-4357/ad9272)

Woo, J.-H., Treu, T., Barth, A. J., et al. 2010, *ApJ*, 716, 269, doi: [10.1088/0004-637X/716/1/269](https://doi.org/10.1088/0004-637X/716/1/269)

Wu, Z., Ho, L. C., & Zhuang, M.-Y. 2022, *ApJ*, 941, 95, doi: [10.3847/1538-4357/ac9cd5](https://doi.org/10.3847/1538-4357/ac9cd5)

Zhao, Y., Ho, L. C., Shangguan, J., et al. 2021, *The Astrophysical Journal*, 911, 94, doi: [10.3847/1538-4357/abe8d4](https://doi.org/10.3847/1538-4357/abe8d4)

Zheng, X., Zhang, Y., & Röttgering, H. 2024, A&A, 686, A169, doi: [10.1051/0004-6361/202347096](https://doi.org/10.1051/0004-6361/202347096)

APPENDIX

A. SURFACE-PHOTOMETRY FITTING

`galight/lenstronomy` fitting results are summarized in Table 5 and fits are shown in Figure 4 and the online figure set. Given the widespread use of `GALFIT` in the literature, `GALFIT` is run for comparison, using the same background subtracted image, error image, PSF and mask (if any). The fitting approach is similar to steps (6–8) described in Section 4. Different starting parameters are used to ensure a true global minimum has been reached. Residuals are visually inspected for best fitting results. Overall, results agree and are robust for the spheroid-only fit in all parameters, as well

as for the magnitudes in the spheroid-disk and spheroid-disk-bar fits (see also, e.g., Benmert et al. 2021). The largest scatter is found for the best-fit Sérsic index for the spheroid component in spheroid-disk and spheroid-disk-bar decompositions. This cautions the sole reliance on Sérsic index to distinguish between classical and pseudo-bulges. Overall, the design of `lenstronomy` (semi-linear inversion and PSO) makes results more robust. Moreover, the automation significantly reduces the user-interaction compared to `GALFIT` to ensure a true global minimum is reached in the fitting process.

Table 5. Surface-Photometry Fitting Results

AGN Name	AGN (mag)	Spheroid (mag)	Disk (mag)	Bar (mag)	η_{sph}	R_{sph} (")	R_{sph} (kpc)	PA_{sph} (")	R_{disk} (")	R_{disk} (kpc)	PA_{disk} (")	q_{disk}	R_{bar} (")	R_{bar} (kpc)	PA_{bar} (")	q_{bar}	
(1)	(2)	(3)	(4)	(5)	(6)	(7)	(8)	(9)	(10)	(11)	(12)	(13)	(14)	(15)	(16)	(17)	(18)
Mrk 335	15.2	15.1	15.7	...	4.4	2.32	1.24	270	0.91	2.9	1.56	265	0.91
Mrk 1501	16.6	16.1	16.3	...	5.0	1.29	2.17	141	0.89	9.75	16.39	176	0.74
Zw 535-012	16.5	16.6	15.6	15.6	1.1	0.58	0.56	170	0.8	16.81	16.19	175	0.53	4.3	4.14	140	0.53
Mrk 590	18.0	15.2	15.2	...	1.5	1.42	0.77	322	0.76	3.2	1.73	50	0.76
Mrk 1044	16.2	15.1	14.6	14.6	1.2	0.77	0.26	162	0.95	12.08	4.09	185	0.88	5.81	1.97	84	0.63
Mrk 1048	19.0	15.0	13.8	...	1.0	2.68	2.33	120	0.69	15.42	13.4	80	0.69
3C 120	15.0	16.2	5.0	2.87	1.95	301	0.97
Ark 120	14.2	13.7	14.7	...	3.7	2.96	1.99	358	0.87	11.6	7.82	21	0.86
NGC 2617	16.2	15.8	13.3	...	1.7	1.24	0.37	20	0.95	12.44	3.72	106	0.95
IRAS 09149-6206	13.0	15.4	15.0	...	1.0	2.44	2.8	47	0.84	9.9	11.34	70	0.65
MCG +04-22-042	16.9	15.5	14.0	16.6	1.3	0.92	0.63	351	0.78	11.67	7.98	353	0.56	7.29	4.98	338	0.2
Mrk 110	16.2	16.6	1.8	1.51	1.1	280	0.96
Mrk 1239	15.0	15.8	15.1	...	1.0	0.99	0.41	151	0.75	4.85	1.99	154	0.75
Mrk 141	18.5	16.2	14.5	16.4	1.0	0.37	0.31	168	0.81	5.99	5.09	139	0.78	3.39	2.88	149	0.31
NGC 3227	14.6	14.2	12.3	...	2.5	1.79	0.14	167	0.64	30.83	2.47	152	0.43
Mrk 142	16.4	17.7	16.9	17.2	1.0	0.41	0.37	17	0.83	7.66	6.94	19	0.82	3.48	3.15	41	0.46
NGC 3516	15.7	13.5	13.1	13.8	1.1	1.96	0.37	234	0.83	16.3	3.05	210	0.83	7.9	1.48	344	0.57
SBS 1116+583A	18.0	17.9	15.9	18.0	1.0	0.59	0.34	68	0.88	4.62	2.67	64	0.88	2.95	1.7	70	0.31
Arp 151	16.9	16.2	16.3	...	2.8	1.21	0.53	155	0.76	5.33	2.31	157	0.37
NGC 3783	14.6	15.2	12.7	15.7	1.0	2.04	0.42	293	0.88	15.15	3.12	160	0.88	12.62	2.6	160	0.19
Mrk 1310	17.3	16.3	15.4	...	4.8	4.2	1.71	308	0.87	4.2	1.71	320	0.73
NGC 4151	13.0	12.4	12.6	...	4.4	6.18	0.44	59	0.87	11.92	0.85	336	0.87
PG 1211+143	14.7	17.0	5.0	0.15	0.24	288	0.59
Mrk 50	16.5	15.3	15.0	...	5.0	4.05	1.98	170	0.8	4.16	2.03	173	0.78
NGC 4593	16.3	13.6	16.6	13.3	1.5	6.21	1.1	97	0.69	39.97	7.07	352	0.48	32.3	5.72	58	0.33
PG 1310-108	15.8	17.5	15.6	18.0	1.0	0.4	0.28	75	0.92	3.68	2.59	77	0.92	1.25	0.88	113	0.39
RBS 1303	15.1	16.1	14.3	15.8	1.1	0.94	0.8	285	0.68	10.39	8.85	288	0.59	4.01	3.42	163	0.45
IC 4329A	14.7	16.7	14.6	...	5.0	1.97	0.63	130	0.9	3.13	0.99	240	0.9
Mrk 279	15.0	14.3	14.6	...	2.1	2.44	1.54	25	0.63	8.67	5.46	65	0.63
NGC 5548	15.0	13.6	14.3	...	3.4	7.85	2.68	86	0.96	15.16	5.18	118	0.87
PG 1426+015	15.7	16.4	1.4	1.99	3.3	53	0.69

Table 5 *continued*

Table 5 (continued)

AGN Name	AGN (mag)	Spheroid (mag)	Disk (mag)	Bar (mag)	n_{sph}	R_{sph} (mag)	R_{sph} (kpc)	PA_{sph} (°)	q_{sph} (mag)	R_{disk} (mag)	R_{disk} (kpc)	PA_{disk} (°)	q_{disk} (mag)	R_{bar} (mag)	R_{bar} (kpc)	PA_{bar} (°)	q_{bar} (mag)
(1)	(2)	(3)	(4)	(5)	(6)	(7)	(8)	(9)	(10)	(11)	(12)	(13)	(14)	(15)	(16)	(17)	(18)
Mrk 841	14.9	15.9	15.4	17.4	1.8	1.27	0.95	104	0.95	6.07	4.53	137	0.95	2.53	1.89	165	0.52
Mrk 1392	16.2	15.7	13.8	15.8	1.4	0.74	0.54	220	0.76	14.04	10.34	228	0.51	4.21	3.1	155	0.47
Mrk 1511	16.6	17.8	14.3	15.7	1.2	0.43	0.3	136	0.94	12.61	8.79	21	0.94	9.49	6.62	161	0.35
PG 1617+175	16.1	17.5	5.0	1.19	2.51	40	0.87
NPM 1G+27.0587	15.8	16.5	14.2	...	1.0	0.61	0.76	204	0.89	6.61	8.16	259	0.78
Zw 229-015	17.7	16.1	15.3	15.5	1.3	0.75	0.43	222	0.79	10.72	6.2	217	0.67	6.33	3.66	215	0.46
NGC 6814	16.2	15.4	12.5	14.8	1.0	1.3	0.14	44	0.93	25.72	2.86	22	0.92	5.25	0.58	28	0.68
RXJ 2044.0+2833	16.0	17.7	15.7	17.2	1.9	0.2	0.2	184	0.89	5.36	5.41	197	0.7	0.98	0.99	142	0.7
Mrk 509	14.1	15.2	15.4	...	5.0	1.84	1.31	70	0.78	2.61	1.86	82	0.78
PG 2130+099	14.9	18.5	17.0	...	3.8	0.34	0.43	57	0.61	2.17	2.75	51	0.61
PG 2209+184	17.3	15.5	16.4	...	5.0	2.85	3.93	99	0.95	3.03	4.19	93	0.87
RBS 1917	16.1	18.6	17.1	...	1.0	0.39	0.51	119	0.9	2.03	2.62	200	0.9
NGC 7469	14.9	14.5	14.2	13.9	1.0	1.44	0.5	87	0.81	29.37	10.22	89	0.81	9.69	3.37	303	0.59

NOTE—Surface-photometry fitting results using `galight/lenstronomy` on HST images. Note that the fitting was done on the original (randomly oriented) images, but all position angles given here are relative to north. Col. (1): AGN Name. Col. (2): Point-source (AGN) magnitude (uncertainty 0.1 mag). Col. (3): Spheroid magnitude (uncertainty 0.1 mag). Col. (4): Disk magnitude (if present; uncertainty 0.1 mag). Col. (5): Bar magnitude (if present; uncertainty 0.1 mag). Col. (6): Spheroid Sérsic index n (5% uncertainty). Col. (7): Spheroid radius in arcseconds (10% uncertainty). Col. (8): Spheroid radius in kpc. Col. (9): Spheroid position angle east of north in degrees (1° uncertainty). Col. (10): Spheroid axis ratio $q (=b/a)$ (0.05 uncertainty). Col. (11): Disk radius in arcseconds (10% uncertainty). Col. (12): Disk radius in kpc. Col. (13): Disk position angle east of north in degrees (1° uncertainty). Col. (14): Disk axis ratio $q (=b/a)$ (0.05 uncertainty). Col. (15): Bar radius in arcseconds (10% uncertainty). Col. (16): Bar radius in kpc. Col. (17): Bar position angle east of north in degrees (1° uncertainty). Col. (18): Bar axis ratio $q (=b/a)$ (0.05 uncertainty). *: For NGC 4533, the HST FOV is too small to cover the entire disk and thus, the disk fit is unreliable.

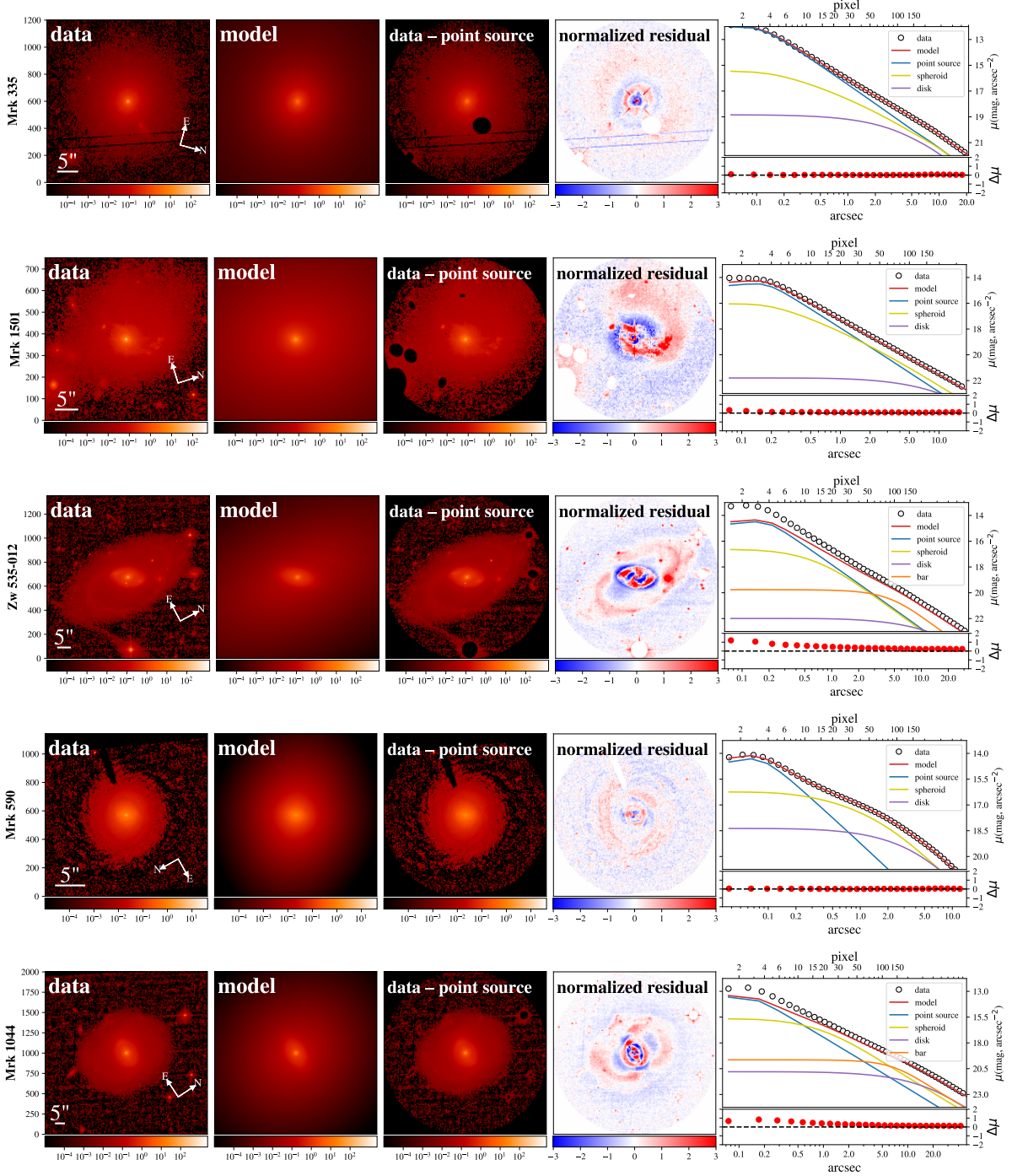


Figure 4. *Surface-Photometry Fits.* From left to right: observed HST image (“data”, including scale bar of 5 arcseconds and North-East directions); best-fit `galight/lenstronomy` model (“model”); PSF-subtracted image (“data – point source”); residual image after subtraction of best-fit model from data, divided by the noise level (“normalized residual”); and surface-brightness profile (data = black circles, model = red line, PSF = blue line, spheroid = yellow line; if present: disk = purple line, bar = orange line). The surface-brightness profile is shown for illustration only, as the fits were performed on the 2D image. Surface-brightness values are given in the plane of the sky (total light within circular aperture; the x-axis is based on a circularized radius). Note that all images are displayed as observed with HST (see Table 1) and fitted by `lenstronomy`. Each row of images corresponds to one object (as labeled on the y-axis of the leftmost panel).

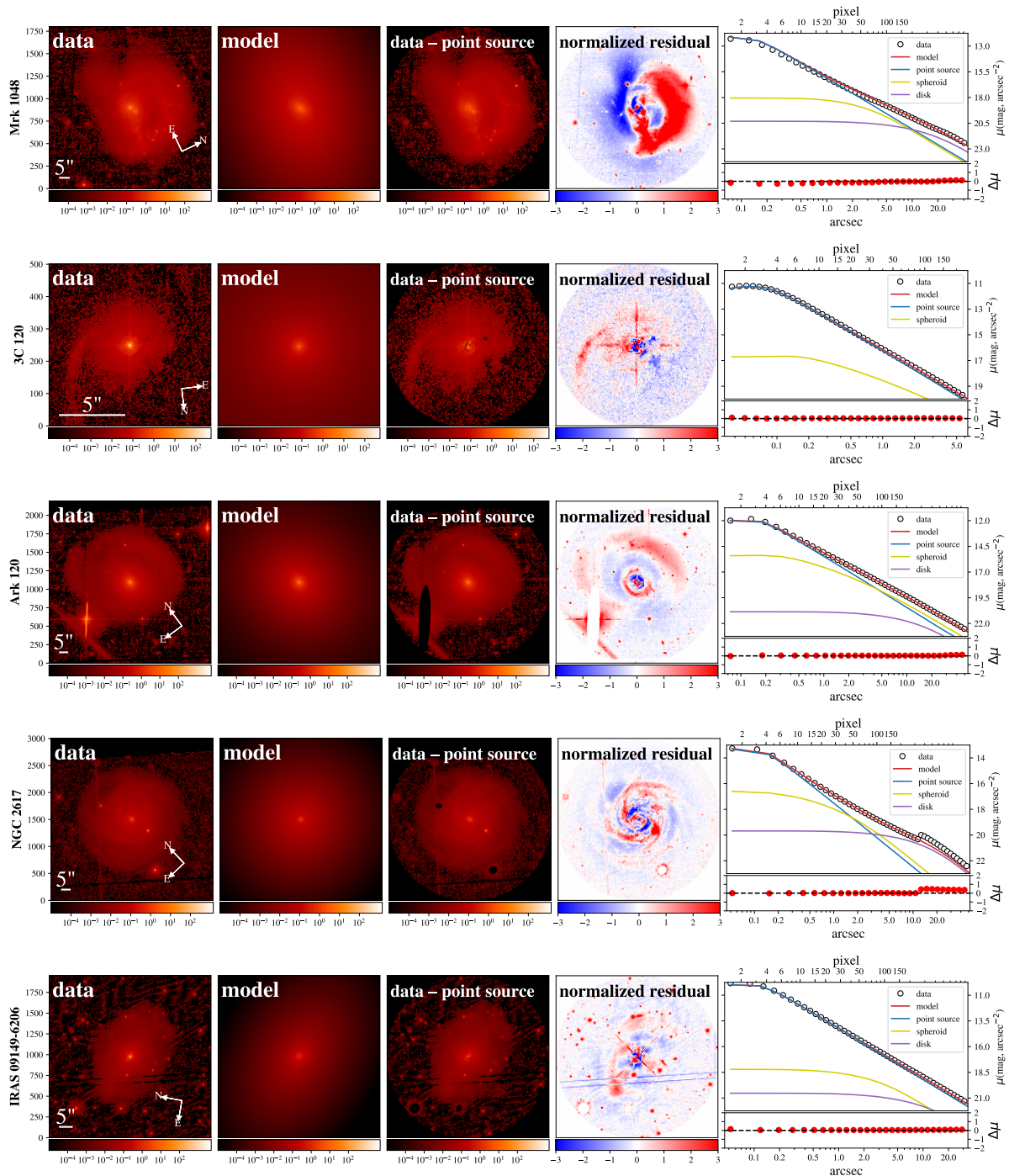


Figure 5. Figure 4 continued.

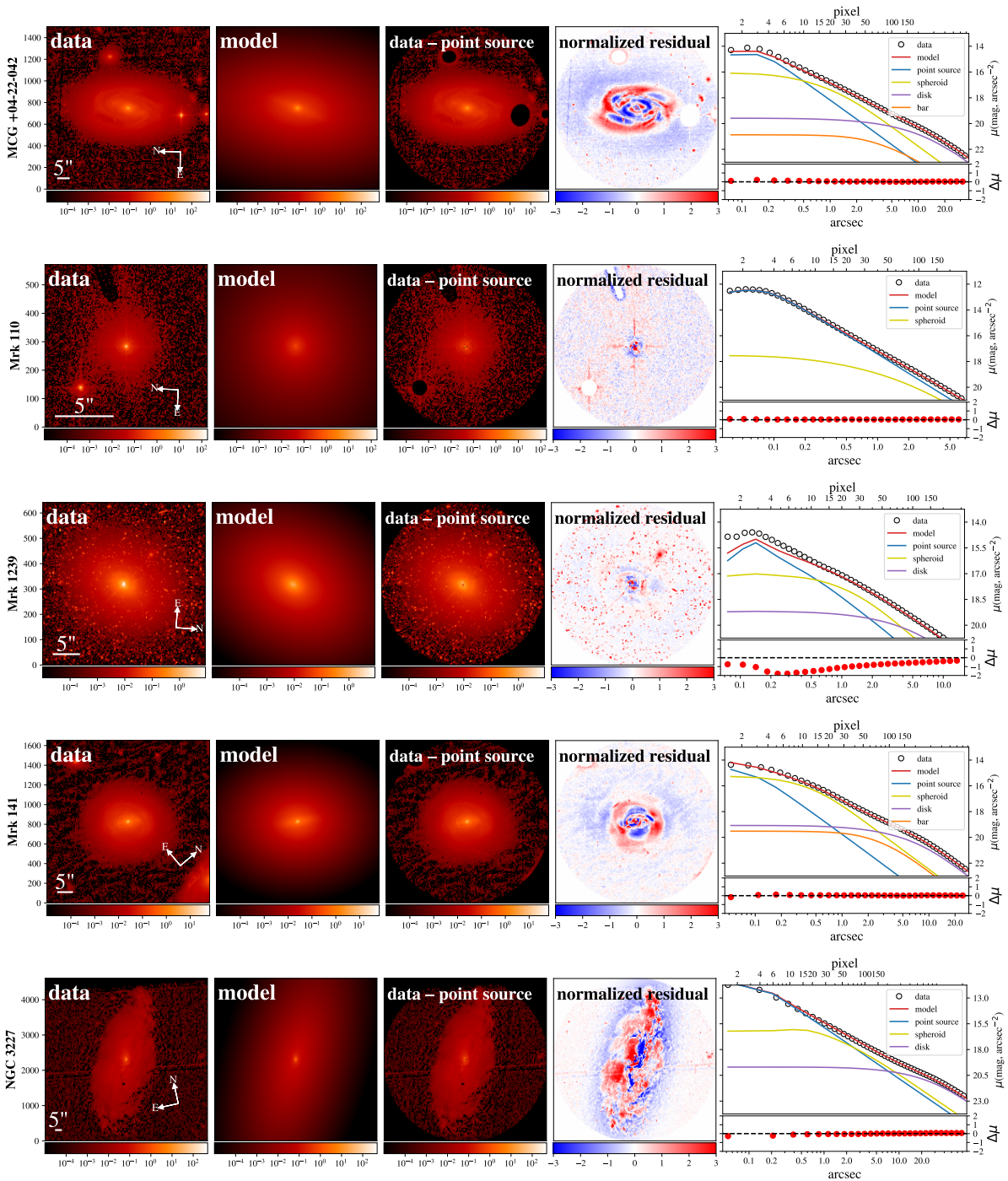


Figure 6. Figure 4 continued.

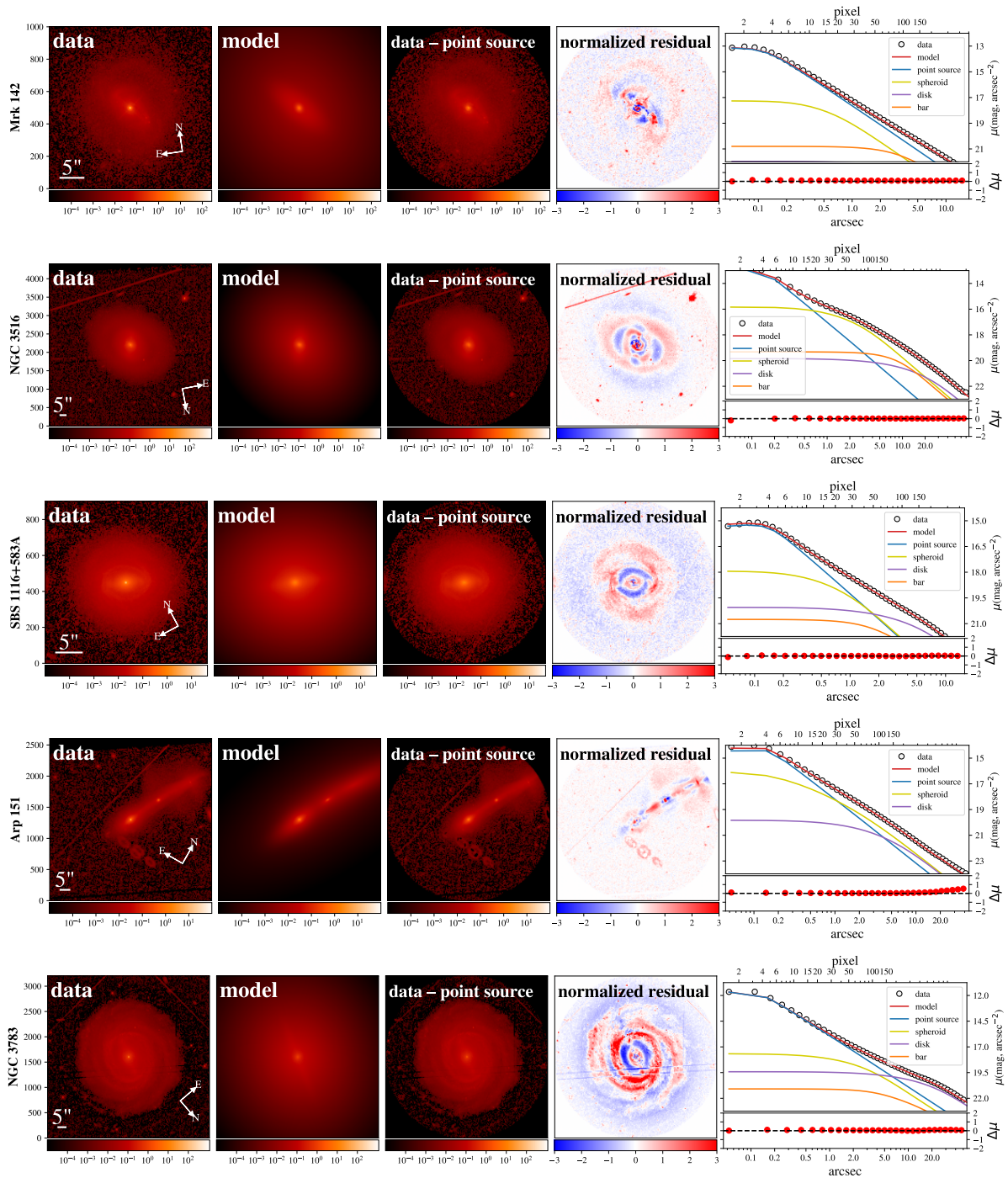


Figure 7. Figure 4 continued.

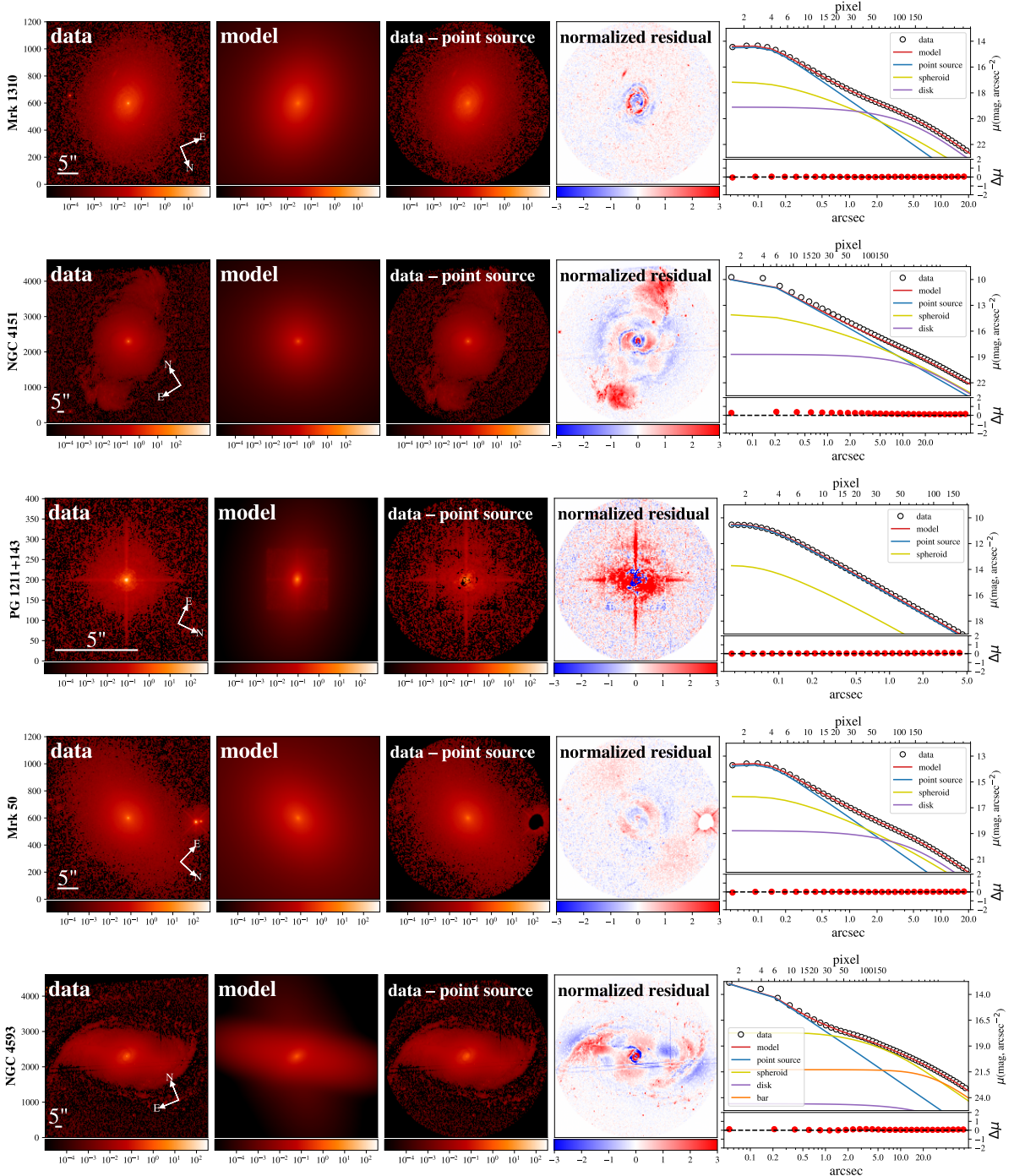


Figure 8. Figure 4 continued.

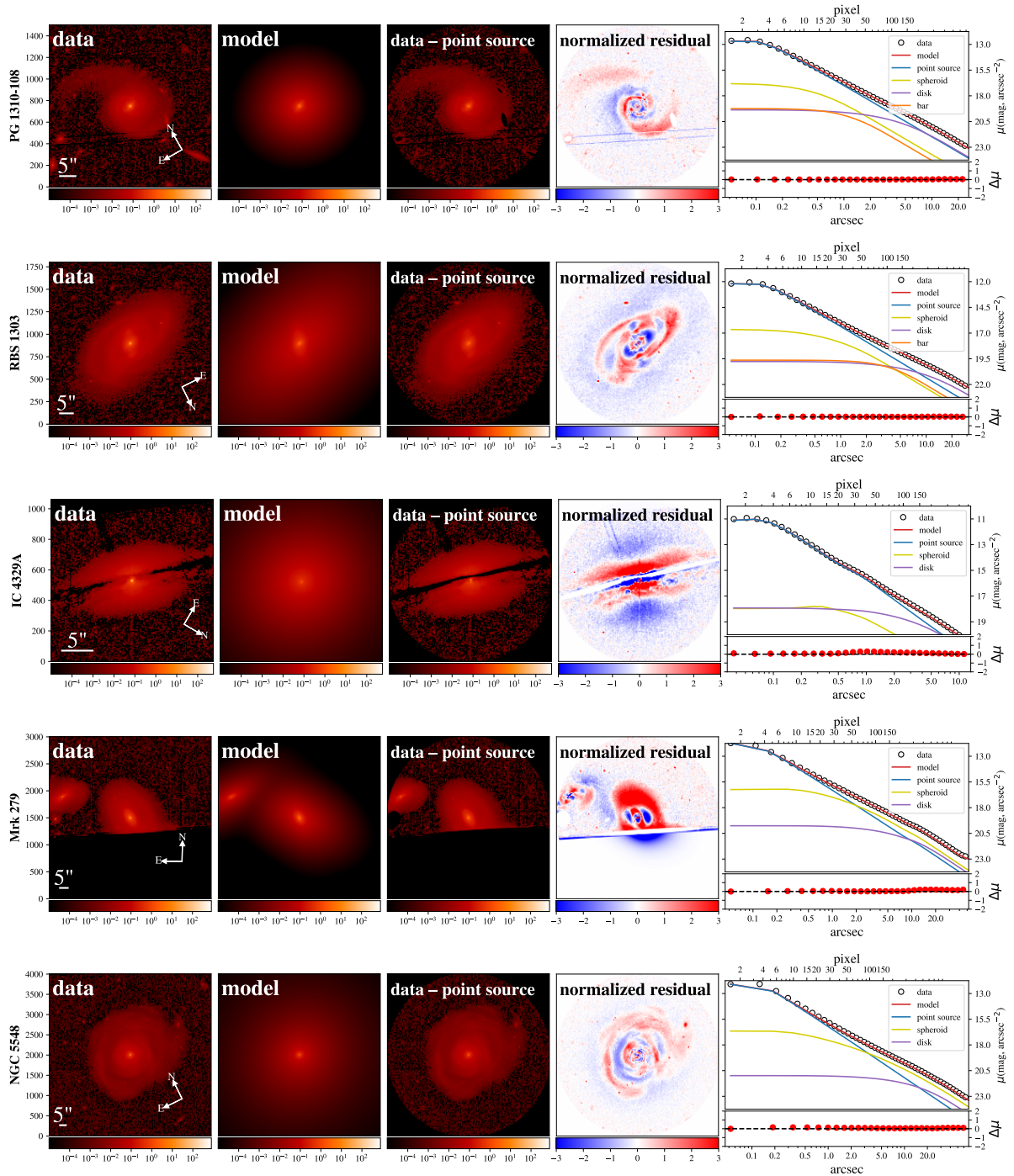


Figure 9. Figure 4 continued.

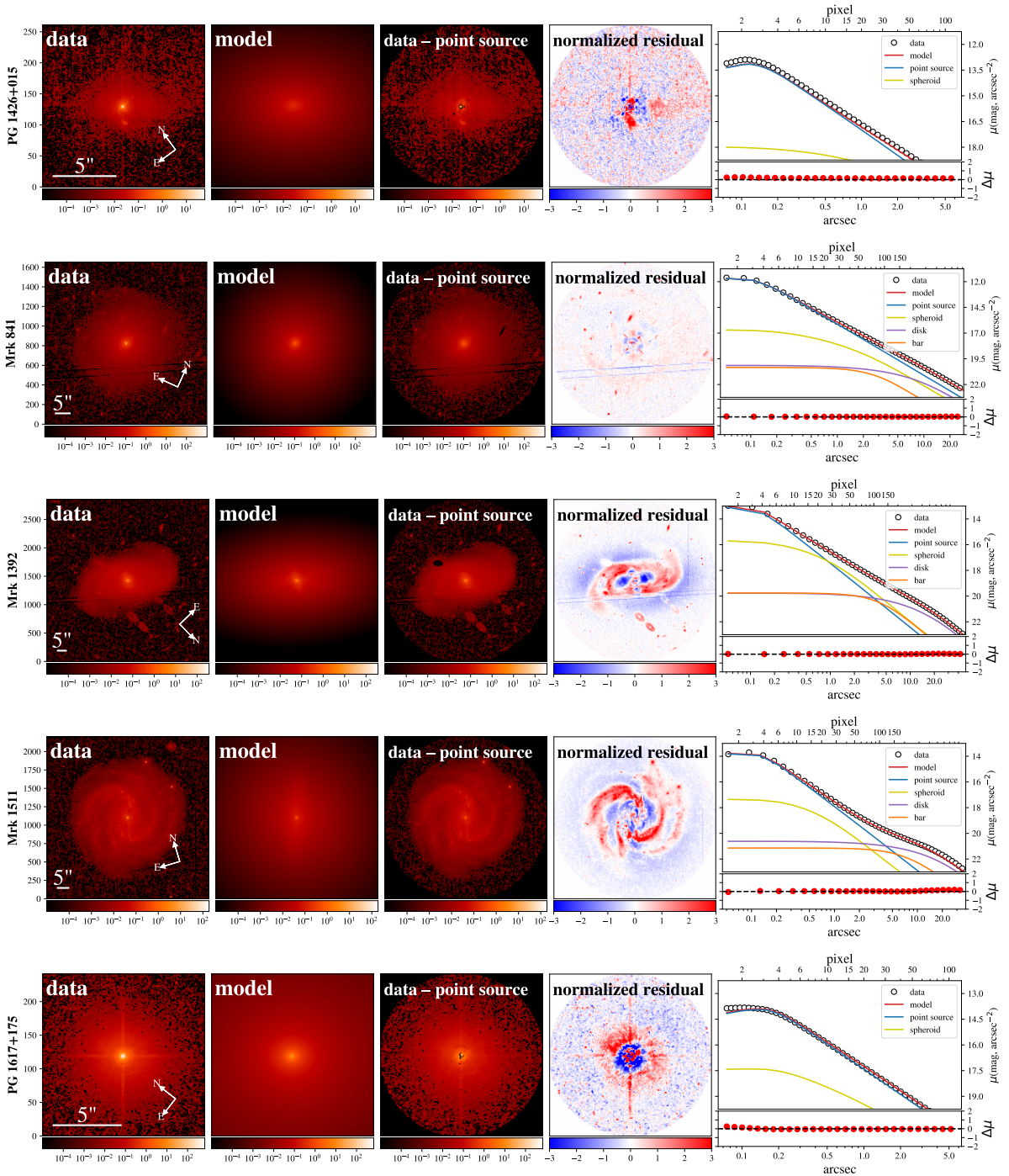


Figure 10. Figure 4 continued.

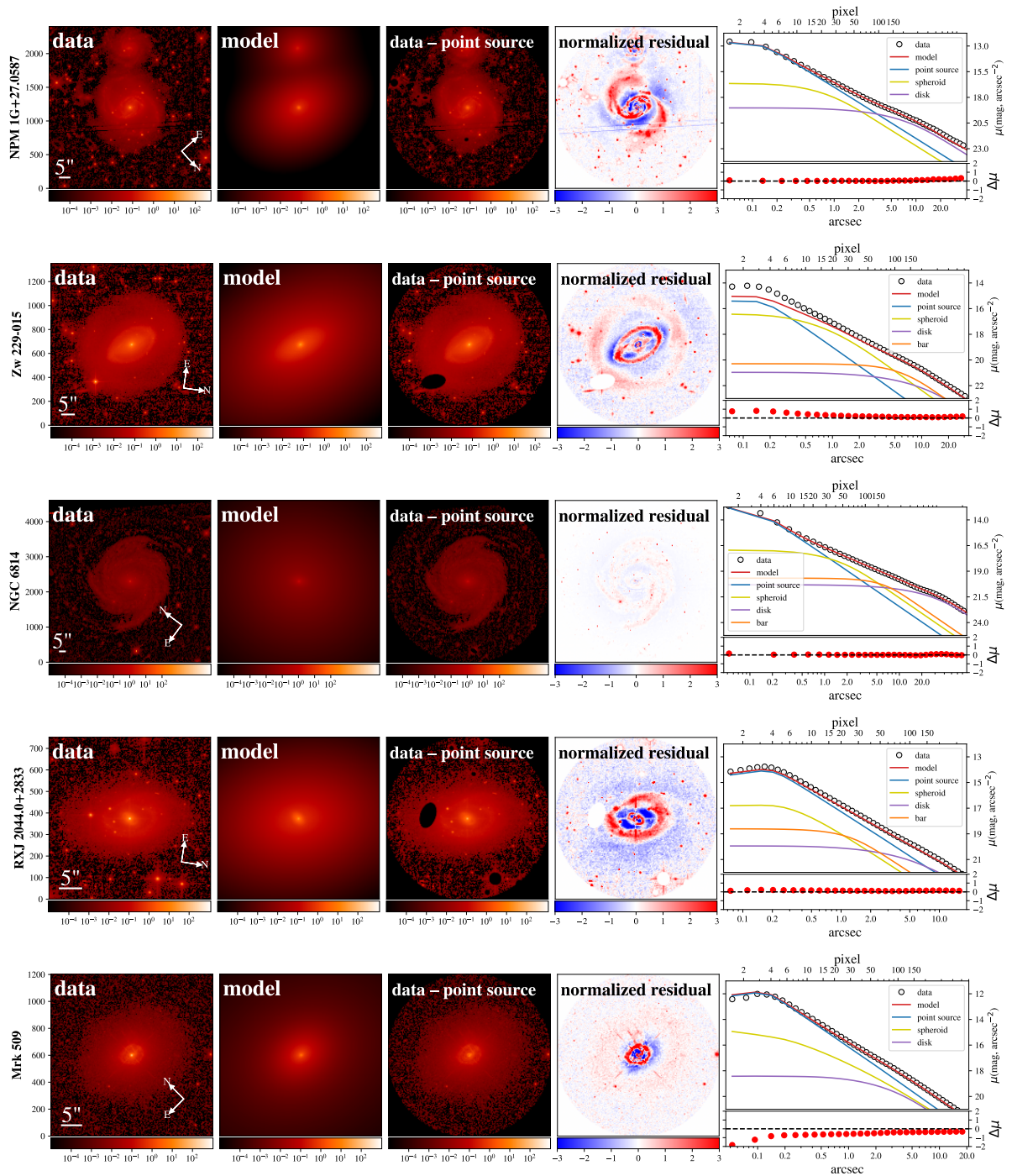


Figure 11. Figure 4 continued.

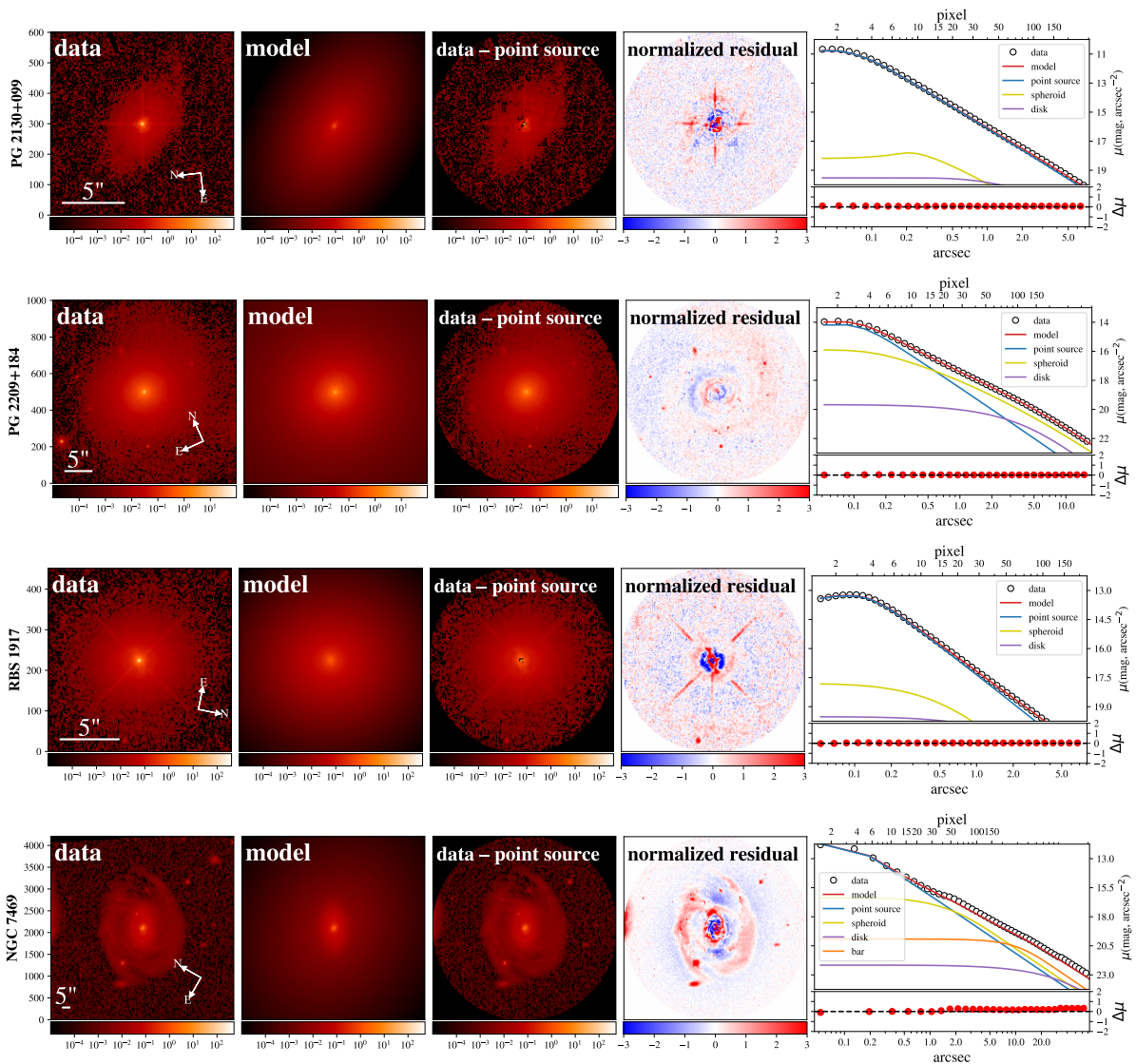


Figure 12. Figure 4 continued.